공학박사학위논문

변형 경화 또는 상전이를 이용한 공압 기반 다중-모드 모핑 소프트 액추에이터

Multi-mode morphing of pneumatic soft actuators using strain hardening or phase transition

2023 년 8 월

서울대학교 대학원

기계공학부

정 한 비

Multi-mode morphing of pneumatic soft actuators using strain hardening or phase transition

Han Bi Jeong

Department of Mechanical Engineering

Seoul National University

A thesis submitted for the degree of

Doctor of Philosophy

August 2023

변형 경화 또는 상전이를 이용한 공압 기반 다중-모드 모핑 소프트 액추에이터

Multi-mode morphing of pneumatic soft actuators using strain hardening or phase transition

지도교수 김 호 영

이 논문을 공학박사 학위논문으로 제출함

2023 년 4 월

서울대학교 대학원
기계공학부
정 한 비

정한비의 공학박사 학위논문을 인준함

2023 년 6 월

위 원 장 : 김 도 년

부위원장 : 김 호 영

위 원 : 박 용 래

위 원 : 이 호 원

위 원 : 이 안 나

위 원 : 정 소 현

Abstract

Multi-mode morphing of pneumatic soft actuators using strain hardening or phase transition

Han Bi Jeong
Department of Mechanical Engineering
The Graduate School
Seoul National University

Soft actuators provide an attractive means for locomotion, gripping, and deployment of those machines and robots used in the fields of biomedicine, wearable electronics and automated manufacturing. In this study, we focus on the shape-morphing ability of soft actuators made of pneumatic networks (pneu-net), which are easy to fabricate with inexpensive elastomers and to actuate using air pressure. As most of pneu-net systems morph into a single designated state, achieving multi-mode morphing has signified multiple inputs of air pressure, making the system highly complex and hard to control. We introduce two pneumatic systems capable of multi-mode morphing using only a single input pressure.

First, we show that by combining pneu-net modules of different materials and geometry, while harnessing the strain-hardening characteristics of elastomers to prevent over-inflation, we can

achieve sequential multi-mode morphing. We provide a theoretical framework to not only predict the shape evolution of pneu-nets as pressure increases, but also design them to sequentially bend, stretch, and twist at distinct pressures. We also show that exploiting the strain-hardening effect and using our design strategy enables a single pneu-net device to carry out multiple functions such as grabbing and turning a light bulb, or holding and lifting a jar.

Second, by embedding a stiffness programmable layer (SPL) into the top wall of a pneu-net, we develop a multi-mode morphing pneu-net using the stiffness difference of solids and liquids by using phase-transition. We first use theoretical analysis of a trilayer beam where the top and bottom beams are made of elastomer. By changing the material in the middle layer (gas, liquid, solid), we show how the effective stiffness changes. For fluids, the middle layer has minimal effect on the effective stiffness of the structure, whereas solids greatly increase the effective stiffness. Then, we experimentally show for a unit cell with an embedded SPL that air and water encapsulated in the SPL can easily deform, whereas ice encapsulated in the SPL can resist deformation at the same pressure. We then proceed to show applications of our idea to achieve multi-mode morphing through using different liquids by using a capillary burst valve to show different designs depending on the liquid's surface tension. Then, we show a cylindrical multi-mode morphing device capable of bending, stretching and forming into different shapes such as a dumbbell. Finally, we show an environmentally-responsive pixelated pneu-net which uses environmental heat to melt specific regions to liquid which enables us to show different shapes and letters when actuated.

Keywords: Soft matter, soft actuator, pneu-net, multi-mode morphing
Student Number: 2017-26227

Contents

List of Figures

Chapter 1

Introduction

1.1 Overview

Soft materials have unique mechanical properties which differentiates soft robots from conventional robots. This thesis demonstrate novel approaches to exploit the advantages of soft robots in the form of multi-mode morphing without increasing the number of input sources for ease of control. In §1.2, we first introduce the research backgrounds and the motivations of soft actuators powered by various stimuli, and focus on the background knowledge of pneumatic actuators in particular. Then in Chapter 2, we demonstrate dual curvature using the strain-hardening effect of elastomer. We present a simple yet versatile design methodology to sequentially morph a soft robot using only a single input source. Through numerical analysis and experiments, we demonstrate sequential multi-mode morphing by controlling material and geometry. Potential applications of our device include a gripper capable of gripping and rotating a light bulb, a self-standing crawler, and sealing then moving a jar from an unwanted environment. In Chapter 3, we present a pneu-net device with an embedded stiffness programmable layer (SPL) to achieve multi-mode morphing using liquid-solid phase transition. Using a simple trilayer beam, we theoretically show the difference of effective stiffness between fluid and solid inside the SPL layer.

Then, we experimentally show how a reprogrammable multi-mode morphing system can be made using phase transition in the SPL layer. We show that an environmentally responsive system can be made to morph numerous times which is unconventional for a pneumatic system using only a single input source. Finally, we summarize our research and provide future works in Chapter 4.

1.2 Backgrounds and motivations

Soft robots are ideal for shape-morphing owing to their flexibility, light weight, and response to external stimuli. This enables them to achieve a variety of tasks, such as grasping delicate objects (Park *et al.*, 2020), moving on various terrains (Hu *et al.*, 2018; Marchese *et al.*, 2014; Shepherd *et al.*, 2011), or changing color for camouflage (Kim *et al.*, 2022; Li *et al.*, 2021a; Morin *et al.*, 2012). The unique mechanical properties of soft materials differentiate from conventional hard materials used in rigid robots, giving it a dominant edge where softness is required. Soft actuators have been driven using various mechanisms such as swelling through chemicals (Lee & Konst, 2014; Wang *et al.*, 2020), thermal responsive materials (Yu *et al.*, 2013; Zhang *et al.*, 2016), using dielectric elastomers (Gu *et al.*, 2017; Pelrine *et al.*, 2000), magnetic responsive materials (Alapan *et al.*, 2020; Dong *et al.*, 2022; Kim *et al.*, 2018), or pneumatically actuated chambers (Hawkes *et al.*, 2017; Shah *et al.*, 2021; Vasios *et al.*, 2020). We introduce various stimuli-responsive soft actuators that change their shape.

Soft actuators using various mechanisms

A chemical responsive soft actuator was developed using elastic organogels synthesized through ring-opening polymerization for shape morphing. A long-chain epoxide monomer is polymerized into a crosslinking fluoro-network. Without any structural design or surface patterning, organic solvents, such as ethanol, can be dropped on the organogel surface to trigger in-situ swelling, leading to shape morphing. Through various droplet placements, different morphologies such as 'V' shape bending, 'S' shape bending, 'rake' shape, 'manta' shape, and 'roof' shape can be achieved (Fig. 1.1A) (Wang *et al.*, 2020).

Using an array of electrodes embedded within thermoresponsive poly(N-isopropylacrylamide) hydrogel, a soft actuator responsive to heat was developed. Depending on the temperature, different portions of a hemispherical shell can swell to change the shape, and deswell when cooled. This leads to the hemispherical shell to buckle and return to its original symmetrical shape after heat is removed (Fig. 1.1B) (Yu *et al.*, 2013).

Actuators responsive to electricity were also developed using dielectric elastomers to produce strains when voltage is applied. Manufacturing a soft actuator with electrodes embedded inside them enables the top electrode to stretch, producing area expansion and thus, shape change (Fig. 1.1C) (Pelrine *et al.*, 2000).

Remote untethered control of soft actuators were developed using change in the magnetic field. Using a magnetic field and magnetic responsive material to make the actuator, various shape morphing can be achieved. Designing magnetically active and inactive segments, an untethered soft crawling robot capable of grasping and moving objects was demonstrated (Fig. 1.1D) (Kim *et al.*, 2018).

Pneumatic networks (pneu-nets) using air pressure for shape morph have also been reported. Using the difference in stiffness of the actuator, pneu-nets can be designed to crawl using bending, roll or climb. A soft robot using multiple pneumatic channels capable of crawling up an inclined surface or rolling side to side has been demonstrated (Fig. 1.1E) (Shah *et al.*, 2021).

However, soft actuators often require a long actuation time, or is difficult to control if morphing complexity is increased. For example, pneu-nets have rapid and powerful actuation, but are only capable of morphing once into a single designated state upon inflation, lacking the ability to morph into different shapes. Therefore, we aimed to preserve the advantage of rapid and powerful actuation of pneu-nets, while increasing the morphing complexity only using a single input, making it easy to control.

Multi-modal morphing systems

Conventional methods of increasing deformation modes and functions of soft actuators have relied on increasing the number of external stimuli (extra pumps, more valves, etc.) (Shah *et al.*, 2021; Vasios *et al.*, 2020) or changing the environment to use different types of mechanisms (Han *et al.*, 2022) have led to higher costs and control complexity.

Similar to inflating a balloon, pneumatic actuators inflate to a final predetermined shape. Increasing the pressure does not result in a different shape, but only increases the degree of morphing (for example, bending angle can change, but the actuator cannot twist). Designing a soft robot by combining multiple pneu-nets and activating each pneu-net separately have been the common approach to achieve multi-modal morphing pneu-nets. However, this approach makes the system more complex and harder to control.

Recently, multi-modal morphing pneu-nets have been developed without using multiple inputs. Using interconnecting tubes to connect individual pneu-nets to each other which is connected to a single pressure supply, sequential morphing can be achieved. By controlling the geometry of the interconnecting tubes and each pneu-net, one pneu-net can activate first, then the air can be moved to the next pneu-net and so forth to achieve sequential morphing (Fig. 1.2A) (Vasios *et al.*, 2020).

Integrating pneu-nets and origami has also been a means to achieve multi-modal morphing. Increasing the pressure to a moderately high pressure will unfold the structure to morph once, then increasing the pressure more will stretch the soft elastic walls, enabling it to morph once more. Applications of this method enables a soft robot to move left first, then right, or can be used as a crawling robot or a gripper (Fig. 1.2B) (Kim *et al.*, 2019).

Using multiple types of stimuli to achieve multi-modal morphing have also been achieved. Using a hybrid material that can respond to both magnetic field change and photothermal stimuli has been developed using superparamagnetic particles and light-responsive joints. The magnetic field is used to exert force on the robot, whereas a light field enables selective deformation of specific joints. Using dual-field coupling manipulation, a crab robot is made to move with high degree of freedom (Fig. 1.2C) (Han *et al.*, 2022).

Another example of using multiple stimuli to achieve multi-modal morphing can be done through using a bilayer that responds to both electricity and humidity. Using hygroscopic contraction and thermal expansion of each layer, the actuator can bend when a voltage is given. Humidity can also be used to activate the actuator to bend. In this case, it can be said that the actuator can bend using either stimuli (Fig. 1.2D) (Amjadi & Sitti, 2016)

Increasing the morphing complexity without to achieve multi-modal morphing without having to use multiple stimuli or increased number of inputs has many advantages. The constraint of having to be in a specific environment, or the issue of high cost in making the system can be a few disadvantages. Also, requiring a lengthy and costly manufacturing process can also be a big downside (Kim *et al.*, 2019). We aimed to develop a soft device that can morph more than once, while keeping the manufacturing process identical to that of a normal pneu-net and only using a single input source to keep control complexity low.

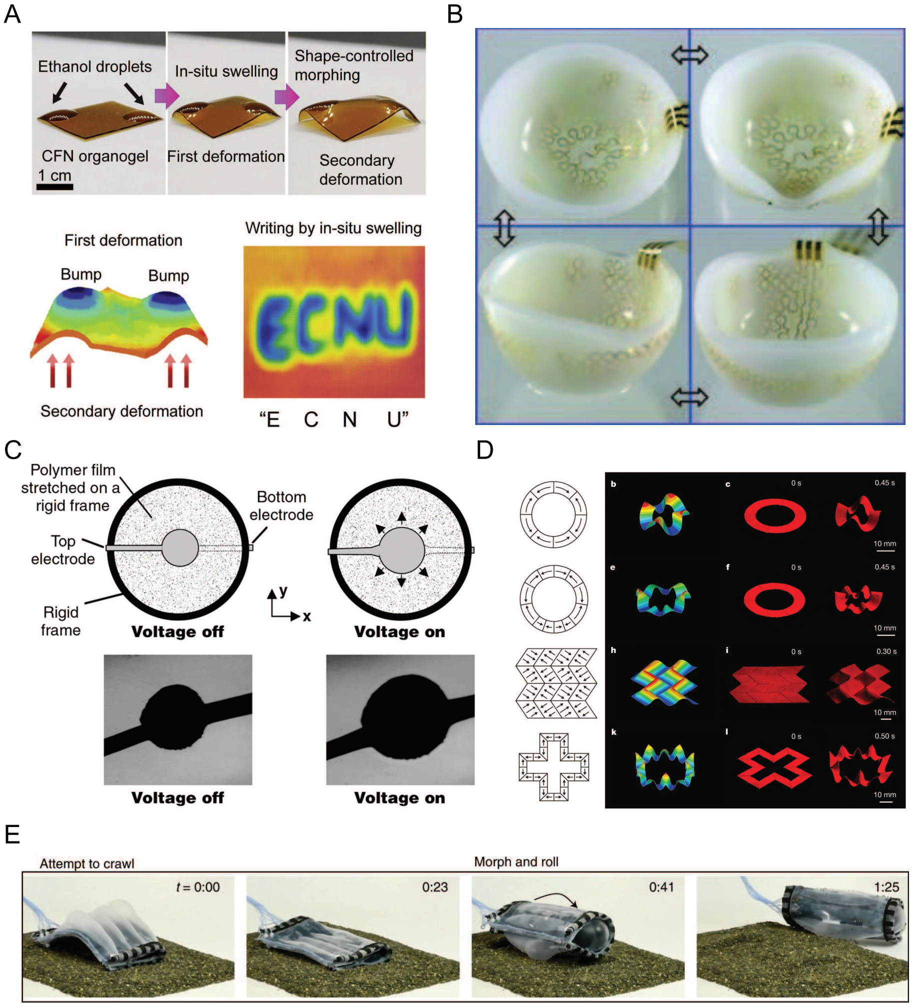

Figure 1.1: Various soft actuators driven by different mechanisms to change their shape. Soft actuators that respond to chemical (A), thermal (B), electrical (C), magnetic (D), and pneumatic (E) mechanisms to change their shape. A, B, C, D, and E are adapted from (Wang *et al.*, 2020), (Yu *et al.*, 2013), (Pelrine *et al.*, 2000), (Kim *et al.*, 2018) and (Shah *et al.*, 2021), respectively.

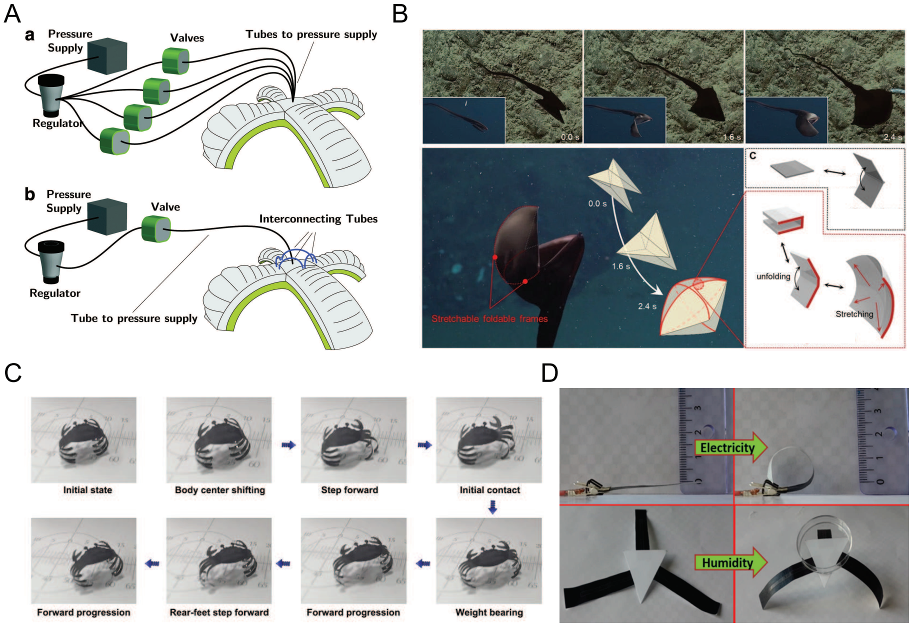

Figure 1.2: Multi-modal morphing actuators using pneumatic actuation and interconnecting tubes (A), origami integrated with pneu-nets (B), magnetic responsive material and photothermal stimulus (C), and a bilayer that responds to both electricity and humidity (D). A, B, C, and D are adapted from (Vasios *et al.*, 2020), (Kim *et al.*, 2019), (Han *et al.*, 2022), and (Amjadi & Sitti, 2016), respectively.

Chapter 2

Multi-mode morphing of pneumatic networks using strain-hardening

Shape morphing soft actuators can be made using different types of materials and respond to numerous stimuli. We focus on soft actuators made of pneumatic networks, which are easy to fabricate with inexpensive elastomers that have fast actuation. It is widely perceived that a single pneu-net morphs into a single designated state, making the pneu-net system complicated to achieve multi-mode morphing. Using only a single input, we achieve multi-mode morphing by combining pneu-net modules of different materials and geometry, by exploiting the strain-hardening effect of elastomers to prevent over-inflation. Using our theoretical model, we propose a design strategy that can be used to sequentially bend, stretch, and twist. We also show various applications such as grabbing and turning a light bulb, and holding and lifting a jar.

In §2.1, we provide a brief introduction to our research. Then, we introduce our mechanical model of hyperelastic elastomers to control the onset of morphing by modulating stiffness in §2.2. By combining pneu-nets of different materials, we use numerical simulations to show how bending–twisting multi-mode morphing pneu-nets can be made and verify them through experiments in §2.3. Then in §2.4, using only a single material, we show that combining pneu-nets of different thicknesses can be used for stretching–bending multi-mode morphing pneu-nets. In §2.5, we combine pneu-nets of different air chamber geometries to show bending–bending multi-mode morphing pneu-nets. Finally, we summarize our research in §2.6.

2.1 Introduction

Shape-morphing of physical objects in response to external stimuli has recently emerged as an essential technology for soft robotics (Dong *et al.*, 2019; Zhang *et al.*, 2021), flexible electronics (Deng *et al.*, 2019; Hao *et al.*, 2022), and smart architecture (Melancon *et al.*, 2021; Wang *et al.*, 2021b). Although novel in artificial systems, shape-morphing has played a pivotal role in survival and prosperity of some animals and most of plants through millions of years of evolution. A number of biological morphing behaviors and structures have already been emulated by artificial actuators, including folding of mimosa leaves (Su *et al.*, 2015; Zheng *et al.*, 2018), snapping of Venus flytraps (Esser *et al.*, 2020; Forterre *et al.*, 2005), circumnutation of tendrils (Gerbode *et al.*, 2012; Must *et al.*, 2019), and bending or coiling of seed awns (Elbaum *et al.*, 2007; Evangelista *et al.*, 2011; Shin *et al.*, 2018). Besides these organisms exhibiting a single mode of shape change, there are creatures capable of multiple modes of shape morphing, which have defied mimicry by soft actuation technologies thus far. For instance, cuttlefish can change into a variety of shapes depending on the surrounding environments for camouflage (Allen *et al.*, 2010, 2014; Panetta *et al.*, 2017), and cone snail can extend its proboscis to paralyze and tether its prey fish, then proceed to engulf it using its rostrum (Olivera *et al.*, 1985, 2015). Just as the multi-mode morphing has conferred extreme flexibility and functionality upon those animals, it would enable unprecedented applications of soft machines, such as multi-purpose transformable soft robots for medical surgery (Piskarev *et al.*, 2022), exploration of unknown environments (Hawkes *et al.*, 2017; Shah *et al.*, 2021), and rescue tasks (Hawkes *et al.*, 2017; Naclerio *et al.*, 2017).

Combining multiple soft actuation systems activated by distinct stimuli (e.g., light and humidity) was demonstrated previously (Li *et al.*, 2021a), but the fabrication and operation processes are complicated, and costly, and thus may lead to defects and errors. Here we present a simple but versatile design methodology to achieve sequential multi-mode morphing of soft machines using a single-input, thereby eliminating complex wiring, plumbing and multiple stimulation devices. Our approach is based on a pneumatic network, which is easy to fabricate, fast in response, capable of generating forces of a wide range of magnitude, and scalable (Melancon *et al.*, 2021).

Our key idea to sequential multi-mode morphing in a simple manner comes from a fact that a softer part in pneu-net will deform prior to a stiffer region when pressurized simultaneously. We also need to make sure that the softer part, which has initiated swelling earlier, does not over-expand in the course of the stiffer part's swelling in order to achieve targeted morphology while preventing disruption. In this work, we provide pneu-net systems with contrast in stiffness embodied by combining networks of different wall thicknesses or materials of different elastic moduli. Over-expansion of softer part is suppressed by exploiting the strain-hardening effect of the softer elastomers, which is tuned to arise at the activation pressure of the stiffer part.

Pneumatic actuators have been researched to create different morphologies rather than using the actuators for its application purposes such as a gripper or a actuator capable to withstanding or applying a certain amount of force. Some examples of shape focused pneu-nets can be seen in Fig. 2.1. Fig. 2.1A shows a pneu-net with multiple input cables which inflate to bend different regions to create different morphologies that can be used to grasp different objects such as a flower, horseshoe shape, or a curvy S shaped

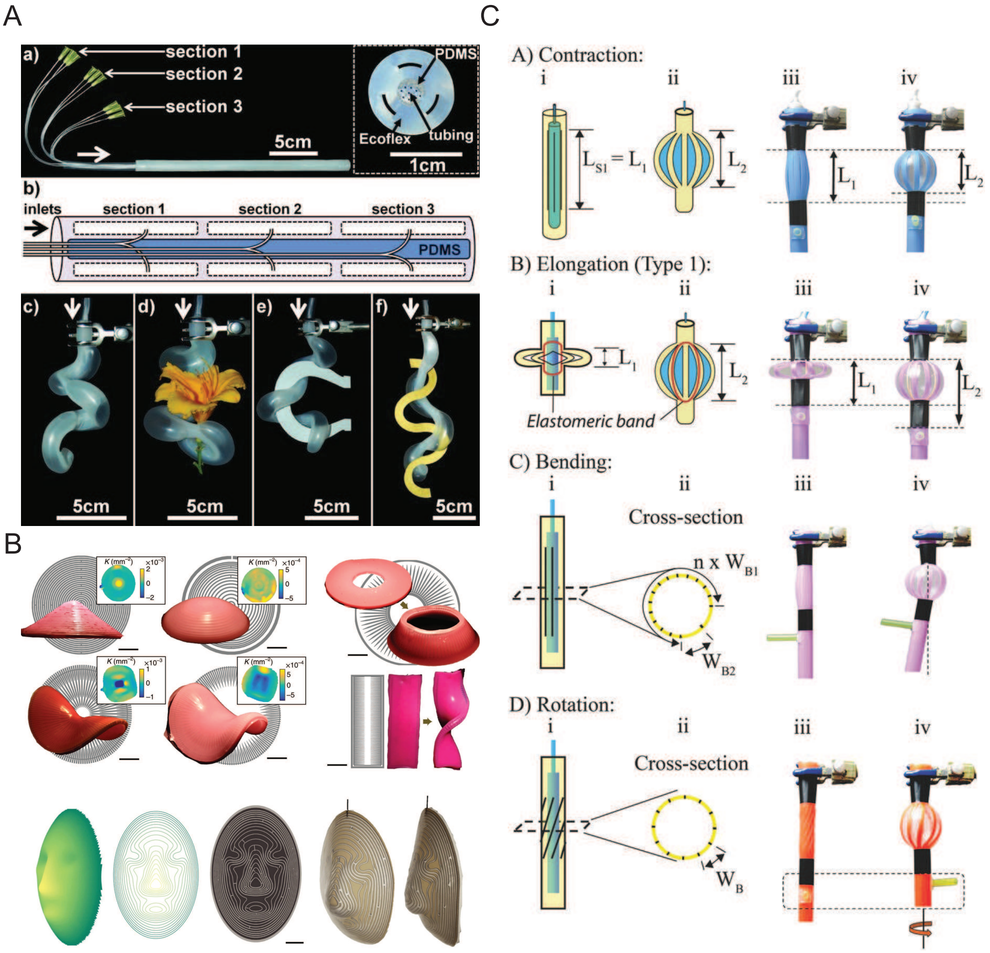

Figure 2.1: Pneu-net actuators focused on shape change have been researched to create (A) multiple curvatures, (B) various morphologies using radial channel density control, (C) and different types of morphing using kirigami. A, B, C are adapted from (Martinez *et al.*, 2012), (Siéfert *et al.*, 2019), (Belding *et al.*, 2018), respectively.

cardboard (Martinez *et al.*, 2012). Fig. 2.1B shows different complex morphologies created by modulating the radial channel density to create shapes like a pyramid or even a human face (Siéfert *et al.*, 2019). Fig. 2.1C shows a pneumatic actuator using kirigami sheets to control how the actuator will morph upon inflation. We can observe that depending on the kirigami design, the actuator can be designed to contract, elongate, bend, or rotate (Belding *et al.*, 2018).

Although these pneu-nets can be used as a gripper such as Fig. 2.1A to hold different objects, the research paper focused on showing shape change through different methods proposed in each paper. They did not conduct any force measurements as their aim was to introduce their approach to create different morphologies using the idea of pneu-nets. Similarly, in the following, we focus on creating a shape morphing pneu-net using a novel approach and introduce some potential applications using our proposed method without any force measurements.

Although we did not conduct any force measurements in the following sections, we can refer to previous research to know the scale of force made from similar silicone based elastomers as the one used in this thesis. We can observe for elastomers Dragonskin 20 and 30 as shown in Fig. 2.2A and B, for the pressure range of 30 - 70 kPa, the block force is in the magnitude of 0.1 to 0.4 N (Sachin *et al.*, 2022). Similarly, the block force for another pneu-net made from Dragonskin 30 was measured using a force sensor shown in Fig. 2.2C which shows a magnitude of blocked force up to 2 N at a pressure of 70 kPa. Depending on the angle of the oblique channels, the blocked force differs which is shown by the colored lines.

Moreover, in table 2.1, a comprehensive force evaluation of different pneu-nets made of different materials was conducted by (**?**). If we observe numbers 1, 2 and 3 in the table, for similar actuator lengths, the resistive force is roughly 1 N between 40 - 80 kPa. For number 4, Dragon Skin 10 at 240 kPa has a resistive force of 3.5 N. If the internal pressure of the actuator is increased, the resistive force will increase as well as the pneu-net will exert a greater force. Therefore, as the elastomers used in this thesis

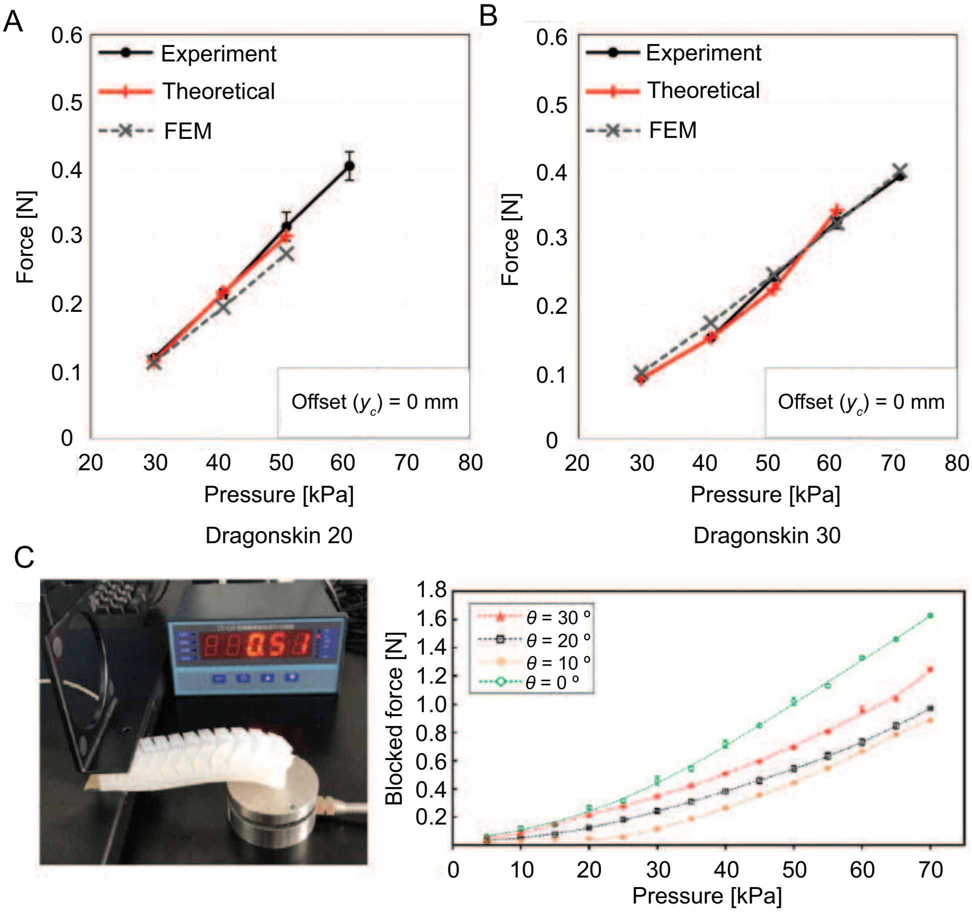

Figure 2.2: Blocked force versus pressure graph for (A) Dragonskin 20 and (B) 30. Blocked force versus pressure for another Dragonskin 30 pneu-net. A and B are adapted from (Sachin *et al.*, 2022), and C is adapted from (Zhang & Oseyemi, 2022).

	Actuator length (mm)	Material	Shore hardness	Internal pressure required (kPa)	Resistive force (N)	Testing procedure
1	88	Dragon Skin 30	30	80	0.4~0.9	Tip force analysis
2	70	Ecoflex 30	30	40	1.04	Pneunet tested on linear rail
3	60	Ecoflex 30	30	80	~1	Tip force analysis
4	60	Dragon Skin 10	10	~240	3.5	Tip force analysis
5	174	RTV2 rubber(Duo-caihani881)	30	80	0.8	Tip force analysis
6	116	RTV2 rubber(Elastosil M4601)	28	43	0.91	Tip force analysis
7	170	Fibre-reinforced RTV2 rubber(Elastosil M4601)	28	60	0.9	Tip force analysis

Table 2.1: Comprehensive force evaluation of PneuNet actuators: A comparative analysis of force output across similar lengths and diverse internal pressure regimes adapted from (Singh *et al.*, 2023).

was mainly Ecoflex 30 and Dragon Skin 10 and 30, we can expect our actuators to exert a similar magnitude of force (scale of 1 N) at a pressure range of approximately 50 - 100 kPa.

In the following, we first explain the mechanical model for the activation condition for a pneu-net, which forms the basis of sequential morphing via strain-hardening. We then present design and demonstration of various multi-mode morphing pneu-nets, including those combining networks of different-modulus materials and of different thicknesses, which can sequentially perform bending-twisting, stretching-bending or bending deformations of opposite curvatures. We show that these multi-mode morphing pneu-net schemes enable a single device to carry out multiple functions with a single pressure input.

2.2 Strain-hardening effect

Some materials exhibit strain-hardening effect, which is the the process of making a metal harder and stronger through plastic deformation. For example, in Fig. 2.3A, the change in modulus or the gradient of a stress-strain curve for manganese steel was observed (Adler *et al.*, 1986). Initially, as strain is increased, stress increases steeply, then the gradient of the stress-strain graph decreases for strain values of approximately 0.12 - 0.18. Then, as strain is further increased to strain values of 0.24 and above, the gradient of the curve increases, which is described as the strain-hardening effect.

Another example can be seen for various metals which show the strain-hardening effect more clearly as we can see in Fig. 2.3B. This graph shows the stress-strain curve for deformed copper, showing a S-shaped curve (Kleemola & Nieminen, 1974). Initially at low strains, stress increases slowly. Then at moderate strain values, stress starts to increase rapidly. Finally, at larger strain values, stress stagnates and increases very slowly. The middle part where stress increases rapidly in comparison to the corresponding strain refers to the strain-hardening effect as the material exhibits

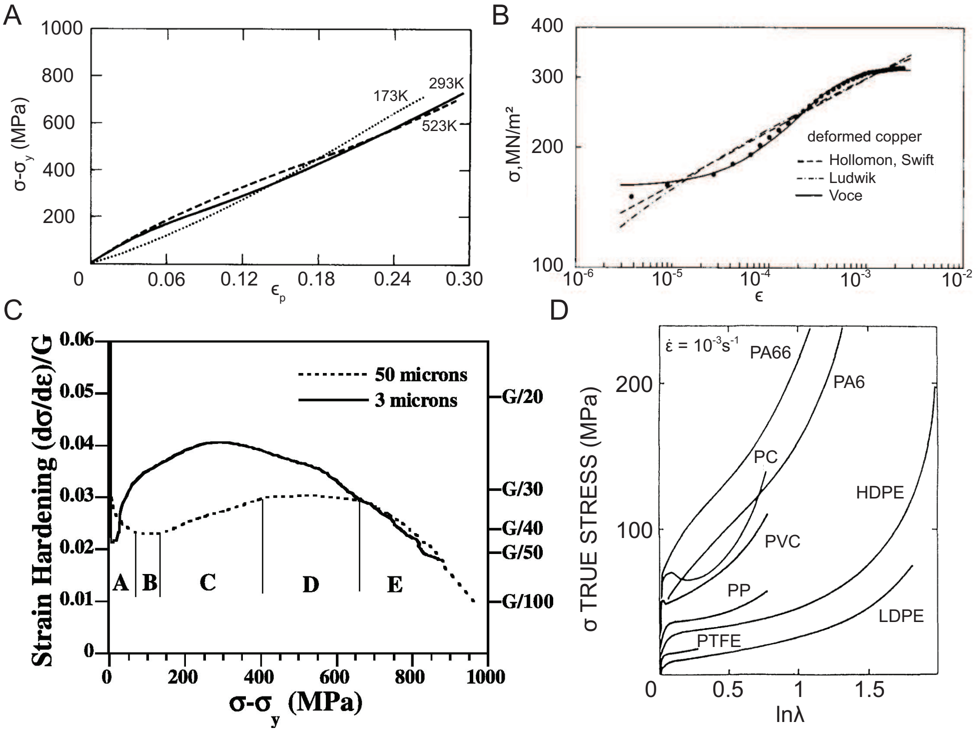

Figure 2.3: Strain-hardening effect observed in (A) manganese steel, (B) copper, (C) steel, and (D) thermoplastics. A, B, C, D are adapted from (Adler *et al.*, 1986), (Kleemola & Nieminen, 1974), (Gutierrez-Urrutia & Raabe, 2012) and (Haward, 1993), respectively.

hardening behavior as strain increases which is evident in the increase in gradient of the stress-strain graph.

Rather than expressing the material characteristic of metals to harden as they are strained through a stress-strain graph, researchers have also shown strain-hardening as stress is increased which is shown in Fig. 2.3C for steel (Gutierrez-Urrutia & Raabe, 2012). We can observe in region B, strain-hardening is increased as stress is increased.

Apart from metals, strain-hardening behavior has also been observed in various thermoplastics as shown in Fig. 2.3D (Haward, 1993). For instance, we can observe the strain-hardening behavior of high density polyethylene (HDPE), where the gradient increases steeply as strain increases which is also evident in other thermoplastics shown in Fig. 2.3D.

Although the term strain-hardening originated from the hardening of metals as it goes through plastic deformation, researchers have observed similar behaviors in other materials such as in thermoplastics. Recently, with the introduction of soft materials and soft robots, similar shapes of stress-strain curves for rubbers and elastomers have been studied, and the term 'strain-hardening' have been applied to newer materials.

Here, we introduce a few soft materials exhibiting strain-hardening behavior, from rubber which is very well known and studied, to relatively new materials.

Stress-strain curve of polyurethane elastomers shown in Fig. 2.4A which shows the material characteristics under tensile strain for pyridinedimethanol (PDM) (Li *et al.*, 2021b). This graph shows the mechanical properties of different R values of PDM. We can observe that except for the black line representing PDM-2.1, the other elastomers all show significant strain hardening which is evident through the increase in gradient of the graph as strain increases. This shows that it gets increasingly harder to produce the same strain as it requires a greater stress, showing that the material hardens with strain. The difference between strain-hardening of metals and soft materials that have been recently developed lies in the amount of strain that is produced. We observe that for the green, blue and red lines, this material is

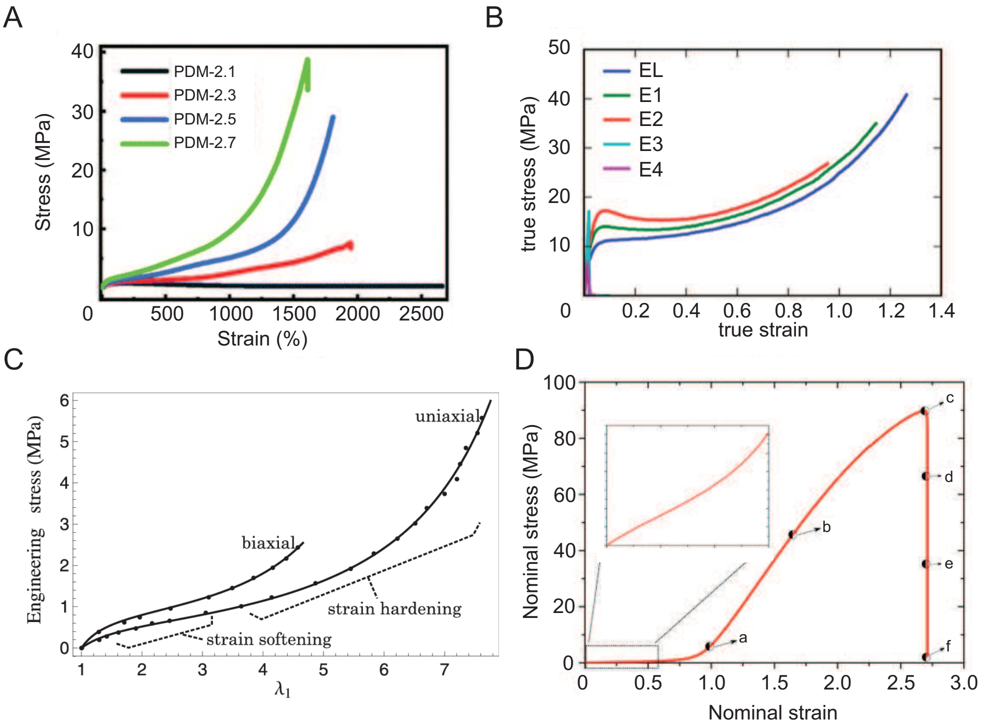

Figure 2.4: Strain-hardening effect observed in (A) polyurethane elastomers, (B) single chain polymer nanoparticles, (C) vulcanized rubber, and (D) rubbery materials. A, B, C, D are adapted from (Li *et al.*, 2021b), (Galant *et al.*, 2019), (Treloar, 1944) and (Swamynathan *et al.*, 2022), respectively.

capable of stretching beyond 15 times its original length, making it suitable to be used as a deformable material for soft robots.

Fig. 2.4B shows the stress-strain curve of single chain polymer nanoparticles with different amounts of crosslinks between them with the lowest degree of intramolecular crosslinks for E1, to the highest for E4 (Galant *et al.*, 2019). The shape of this graph is in the shape of a S-shaped curve which has the characteristics of undergoing regions of strain-softening (requires less stress to produce the same strain) and strain-hardening (requires more stress to produce the same strain). Initially, the material requires a large amount of stress to produce even the smallest strain. Then, the material undergoes region of strain-softening which is evident by looking at the decrease in gradient. As strain is increased to values beyond 0.6, we can observe the gradient increasing back up, showing its strain-hardening properties.

The strain-hardening properties of rubber is very well known and studied which we can see through Fig. 2.4C, which clearly explains the different characteristics of vulcanized rubber (Treloar, 1944). This research was published a long time a go, showing that the S-shaped curve and the property of rubber which undergoes regions of strain-softening and hardening was well studied. We can see that this shape is similar in the sense that it has regions of gradient decreasing and increasing as the one shown in Fig. 2.4B, which shows that although the material is different, they exhibit similar properties.

Last but not least, Fig. 2.4D shows a nominal stress versus strain curve for rubbery materials which also show the S-shaped behavior as mentioned above (Swamynathan *et al.*, 2022). Depending on the strain of rubbery materials, the material exhibits different properties which can be used to our advantage.

From these examples, we can see how the term 'strain-hardening' started from metals and rubbers, but are now being used to describe the stress-strain S-shaped curve of soft elastomers that have been recently introduced and developed. In this chapter, we refer to the increasing in the gradient of a stress-strain curve, or requiring a larger strain to produce the same strain, as the strain-hardening behavior which is applicable to elastomers. Using hyperelastic models which are commonly used to show these behaviors in hyperelastic elastomers, we design soft actuators to morph more than once by utilizing this trait in the form of pneu-nets.

2.3 Elastomer characteristics

From the section above, we showed the strain-hardening properties of elastomers. In this section, we will discuss on the other properties of elastomers used to make our actuator (Ecoflex, Dragonskin elastomers) such as its viscoelastic properties and its performance under cyclic tests.

First, let us observe cyclic tests conducted by Laio et al. for the commercial elastomer Ecoflex 30 which is shown in Fig. 2.5A (Liao *et al.*, 2020). This stress-strain graph shows three lines, with the black line showing the behavior of Ecoflex 30 under pre-stretch condition, red line under relaxation, and blue line under 100 cycles. If we compare the black and red lines, we can see that apart from the very end of the curve, they have almost identical paths. For the blue line where it was a cyclic test up to strain value of 3 for 100 cycles, we can see that the curve moves slightly downwards with each cycle, but does not show drastic change in the curvature of the overall graph. We can actually observe the stress-strain curve converging, and no residual stress was observed after unloading. From these results, we can see that for the commercial elastomer Ecoflex 30 for strains up to 3, cyclic tests do not show drastic change in the shape and behavior of the elastomer by observing the stress-strain graphs.

Next, let us observe cyclic tests conducted by Li et al. for a composite elastomer of Dragonskin 20 and Ecoflex 30. From Fig. 2.5B (Li *et al.*, 2020), we can see that the composite elastomer is made up of a net of stiff material (Dragonskin 20) which is shown as the pink material, and the rest of the voids filled with a softer elastomer of Ecoflex 30. From the stress-strain graphs of this composite material for strain up to 2, we can hardly see the

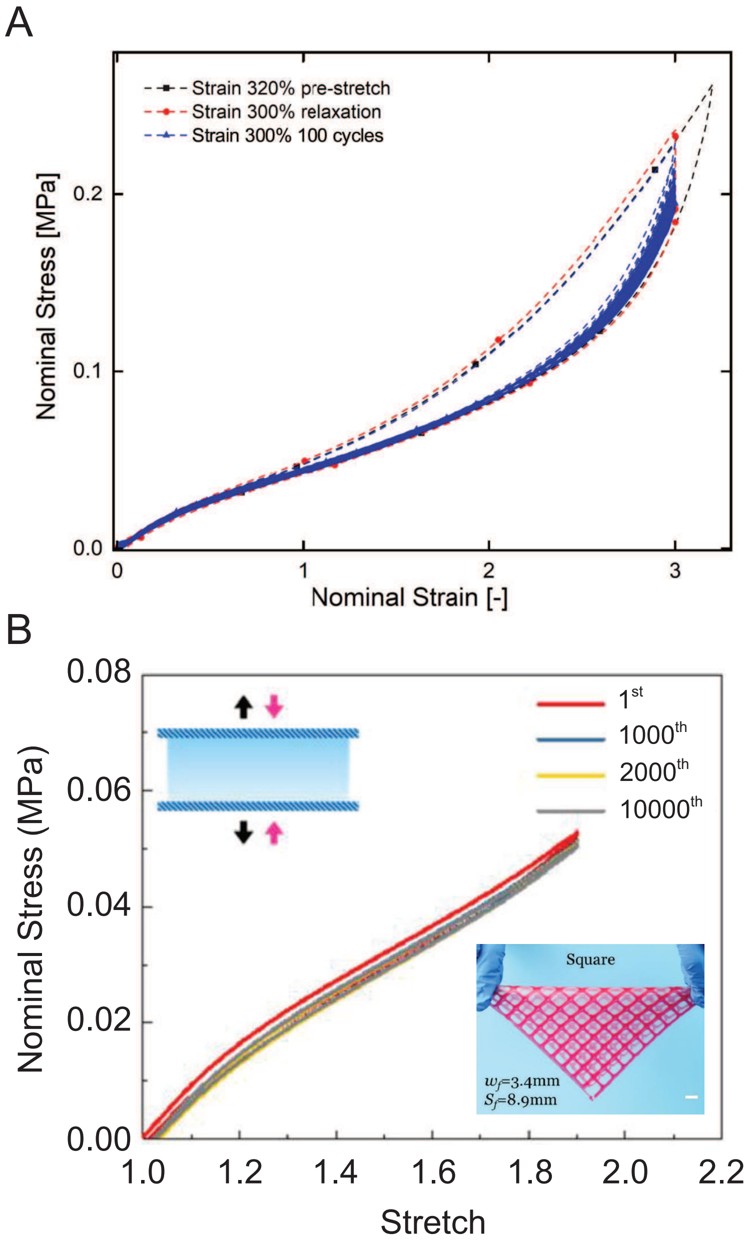

Figure 2.5: Cyclic test for (A) ecoflex 30 and (B) composite elastomer. A, B are adapted from (Liao *et al.*, 2020) and (Li *et al.*, 2020), respectively.

change in its curve up to 10,000th cycle. They also reported slight signs of residual strain, but we can see that it is a very small amount considering the material has been stretched for 10,000 times.

We observed the effect of cyclic tests for commercial elastomers which are used in this thesis to show that for strains up to 3, elastomer properties do not change drastically and remain relatively the same for cycles up to 10,000 times. Although the effect of cyclic tests may depend on the strain value the experiment was conducted for, the experiments conducted in the following sections were conducted in the strain range of approximately 2 to 3. We may then assume that the effect of cyclic actuation of our actuators have minimal effect on the morphing curvature and geometry.

Next, let us look at the effect of temperature on commercial elastomers upon actuation. Experiments conducted for the commerical elastomer Ecoflex 50 at different drastic temperatures are shown in Fig. 2.6A (Lavazza *et al.*, 2023). The experiment was conducted for a wide range temperatures varying from negative 40 °C to 140 °C for large strain value of up to 6 and 8 depending on the temperature. Lavazza et al., reports that the glass transition temperature of Ecoflex is negative 33 °C. At low temperatures of -40 °C to -20 °C, the stress-strain graph shows a steeper gradient and thus would require a greater pressure to produce the same deformation. For temperatures at around room temperature, the light green line shows a lower gradient curvature. For high temperature ranges of 80 °C and above, the elastomer exhibits a stress-strain curvature that is similar to that conducted in room temperature. Although there are differences in the stress-strain graphs depending on the temperature of Ecoflex 50, the difference in each curve does not drastically change.

For stress-strain experiments conducted for the commercial elastomer Ecoflex 30 which is shown in Fig. 2.6B (Liao *et al.*, 2020), for the same temperature range explained above, we can observe the stress-strain graphs for loading and unloading. At low temperatures of -40 °C to -20 °C, the elastomer shows the highest peak at its maximum strain in comparison to all other temperatures, but have similar loading and unloading paths as

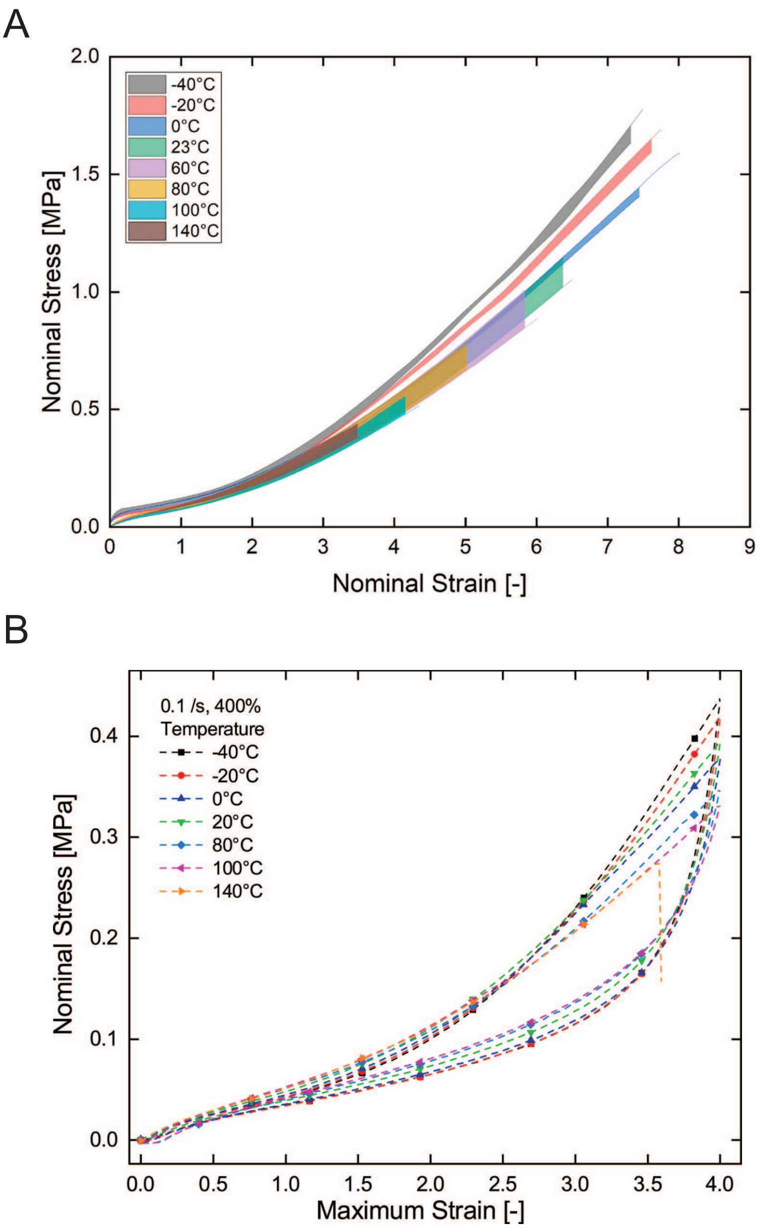

Figure 2.6: Stress-strain curves for commercial elastomers (A) Ecoflex 50 and (B) 30 conducted at different temperatures. A, B are adapted from (Lavazza *et al.*, 2023) and (Liao *et al.*, 2020), respectively.

the rest. When temperature is increased, we can observe that the stress-strain graph has lower nominal stress at the same maximum strain, but still follow similar loading and unloading paths no matter what temperature the elastomer is in.

From these results, we can state that although temperature affects the stress-strain curvature of commercial elastomers, they do not have massive impact on their material properties as they have similar curves and loading and unloading paths. There would be a slight difference in stretching the same elastomer at the same pressure depending on temperature, but the difference would not be too large. For all experiments conducted in the following sections, our pneu-nets were actuated between -20 °C and room temperature. Thus, we can say that temperature range conducted in our experiments have minimal impact in deciding the morphing shape of our pneumatic networks.

Next, we look at the mechanical property of rubbers when exhibiting the strain-hardening effect. In Fig. 2.7A (Cantournet *et al.*, 2009), we can observe the stress-strain curve for rubber that is being stretched for the first time (referred to the virgin curve) and being restretched after removing the load. Cantournet et al., introduces this effect as the Mullins effect (Beatty & Krishnaswamy, 2000), which is the deformation-induced microstructural damage due to rupture of molecular bonds within the rubber. These ruptured bonds reform to create a new microstructure which ultimately leads to stress-softening. We can observe from Fig. 2.7A that the virgin curve has a much higher stress at low strains whereas after the initial stretch, it has a lower curve at lower strains upon loading.

As we introduced the strain-hardening effect as requiring more stress as strain increases, we can identify the stress-strain curve after initial loading more suitable to use for its strain-hardening behavior. To use the strain-hardening behavior, all experiments conducted in the following section was initially stretched to transform the stress-strain curve from the virgin curve to its restretched state.

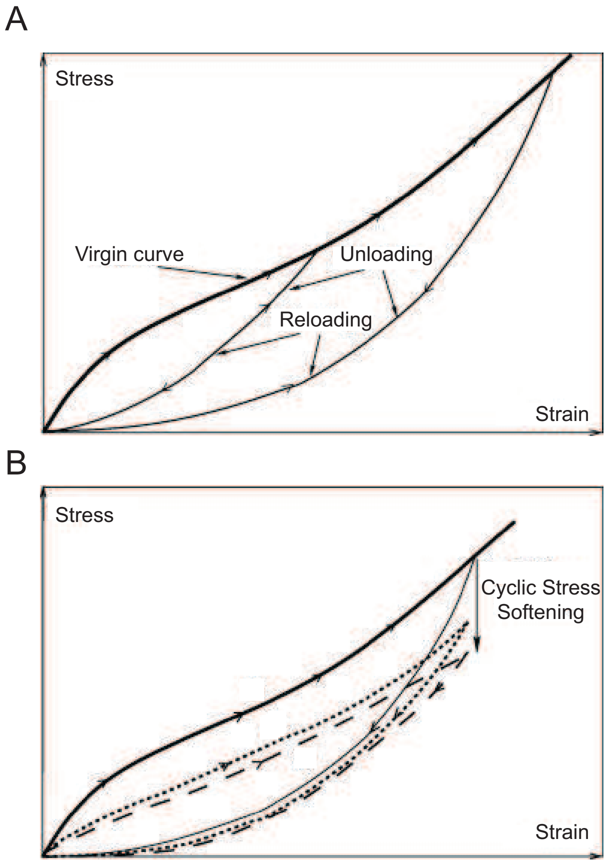

Figure 2.7: Stress-strain curves for cyclic stress softening due to Mullins effect (A) after virgin curve, and (B) repetitive stress softening. A, B are adapted from (Cantournet *et al.*, 2009).

Similar to the previous section referring to cyclic experiments of commercial elastomers, Fig. 2.7B shows the cyclic stress softening effect of rubbers. After repeatedly loading and unloading, the stress-strain curve converges to a single line which shows that after a few cycles, the behavior of the rubber would be similar unless stretched to a whole different strain to further rupture the bonds. The dissipative microstructures, clusters of chain molecules held by interatomic forces and molecular chain entanglements leads to stress-softening.

Last but not least, let us observe the effect of viscoelasticity, or the strain rate on the stress-strain curve of commercial elastomer Ecoflex 30. In Fig. 2.8A (Liao *et al.*, 2020), we can observe the behavior of Ecoflex 30 on different strain rates ranging from 0.0001 per second to 0.1 per second for strain of 4. Without any pre-treatment of pre-stretch (virgin curve), we can observe that the faster the elastomer is stretched, the higher the stress-strain curve gets which is evident by looking at the black line in comparison to the green line. The overall shape looks the same, with different gradients as strain is increased.

However, this effect can be nullified by pre-treating the elastomer by pre-stretching it for 10 cycles to strain of 4 at a rate of 0.1 per second as shown in Fig. 2.8B. We can observe that the black line referring to strain rate of 0.1 per second and red line referring to 0.001 per second being almost identical. This shows that the Mullins effect is very important in deciding the stress-strain curve for rubbers and elastomers. Thus, after an elastomer has been stretched once, the material properties, mainly the stress-strain curve, does not change by a significant amount. This makes it reliable to conduct experiments using elastomers that have already been stretched at least 5 times to the strain value that was design to stretch the elastomer for use.

In the following section, all experiments were thus conducted not using their virgin curve, but by stretching the pneu-net at least 5 times before recording or conducting and experiments to ensure the repeatability of the

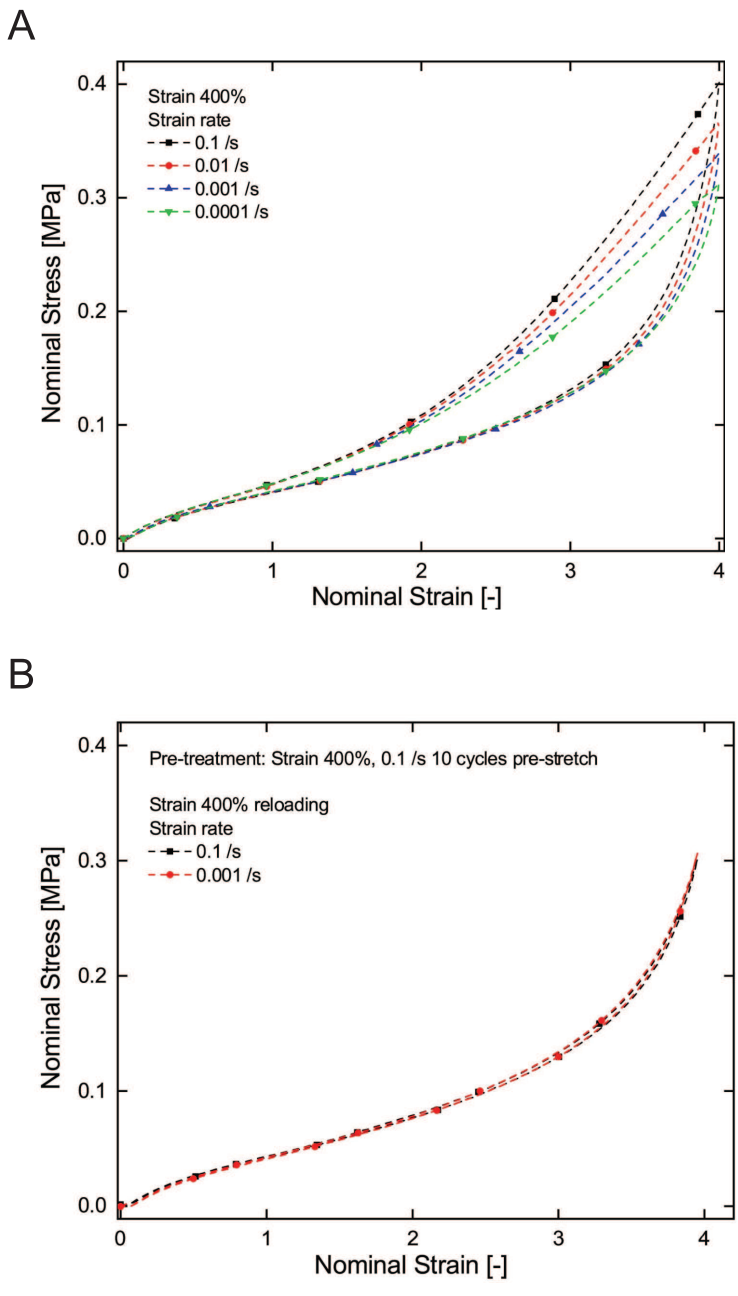

Figure 2.8: Stress-strain curves of commercial elastomer Ecoflex 30 depending on (A) strain rate, and (B) strain-rate after pre-stretch. A, B are adapted from (Liao *et al.*, 2020).

results introduced henceforth. We would also like to mention that increasing the elastomer to a value that is much greater than the pre-stretch strain would result in a different material property that would likely rupture the molecular bonds, resulting in a different result than previously stretched. It is important to keep the strain range the same when conducting experiments using the strain-hardening effect as this could greatly affect the results.

2.4 Mechanical model

As a simple model to describe how we control the onset of morphing by modulating stiffness (determined by dimensions and elastic modulus) of a pneu-net, we consider a unit cell that can bend about the x-axis upon pressurizing, as shown in Fig. 2.9. We design depth to be much longer than width, to ignore bending about the y-axis. When unactivated, the cuboid air chamber having width w_c, height h_c, and depth d_c is surrounded by top and bottom walls of thickness h_t and h_b, side walls of identical thickness w_s, and front and rear walls of identical thickness d_f. The entire cell consisting of the air chamber and the surrounding walls has width $w = w_c + 2w_s$, height $h = h_c + h_t + h_b$, and depth $d = d_c + 2d_f$. We assume that all the walls have the same shear modulus μ except the bottom wall of a higher modulus μ_b. Then the cell with $d \gg w$ deforms as shown in Fig. 2.9(b) when the inner chamber is pressurized.

The deformation behavior of the cell is represented by a curvature κ, which is defined by $\kappa = \theta/d$ with θ being the central angle of the bent cell, as shown in Fig. 2.9(B). The curvature κ is determined by the cell dimensions and material properties when the pressure p is applied, so that we write $\kappa = F(w_s, w, d_f, d, h_t, h, \mu, p)$, where we assume that the modulus and thickness of the bottom wall is kept constant and that all the walls are incompressible with Poisson's ratio of 0.5. For geometrically similar cells with constant ratios of w/d and h/d, the dimensionless curvature, κd, can be expressed

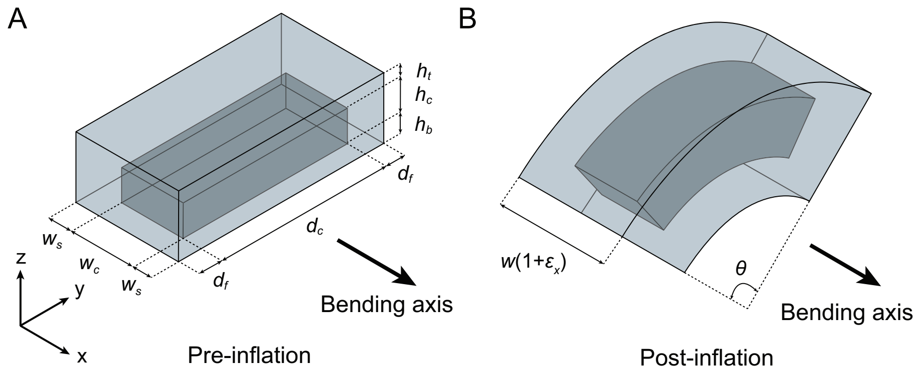

Figure 2.9: Schematics of a unit cell in its (A) pre-inflated and (B) post-inflated states.

as a function of four dimensionless variables using Buckingham's pi-theorem (Buckingham, 1914): $\kappa d = f(w_s/d, d_f/d, h_t/d, p/\mu)$.

We can express the total energy of a unit cell as shown in Fig. 2.9A made of a hyperelastic elastomer with strain-hardening effect by using the incompressible Gent model (Gent, 1996) to express the stored strain energy density function as

$$U = -\frac{\mu J}{2}\log\left(1 - \frac{I_1 - 3}{J}\right), \tag{2.1}$$

where μ is the elastomer shear modulus and I_1 is the first strain invariant which can be calculated by the right Cauchy-Green strain tensor for each wall. J is the maximum of I_1 where the material cannot stretch further as it has been fully stretched. Then, the total energy of the pneumatic channel can be expressed as

$$U = U_p + U_b^{\text{bottom}} + U_s^{\text{depth}} + U_s^{\text{height}} + U_s^{\text{width}}, \tag{2.2}$$

where U, U_p, U_b, and U_s respectively denotes the total energy, the energy from internal pressure, the bending energy, and the stretching energy.

Figure 2.10A and B respectively show the experimentally measured curves of stress–strain and elastic modulus–strain for the materials used

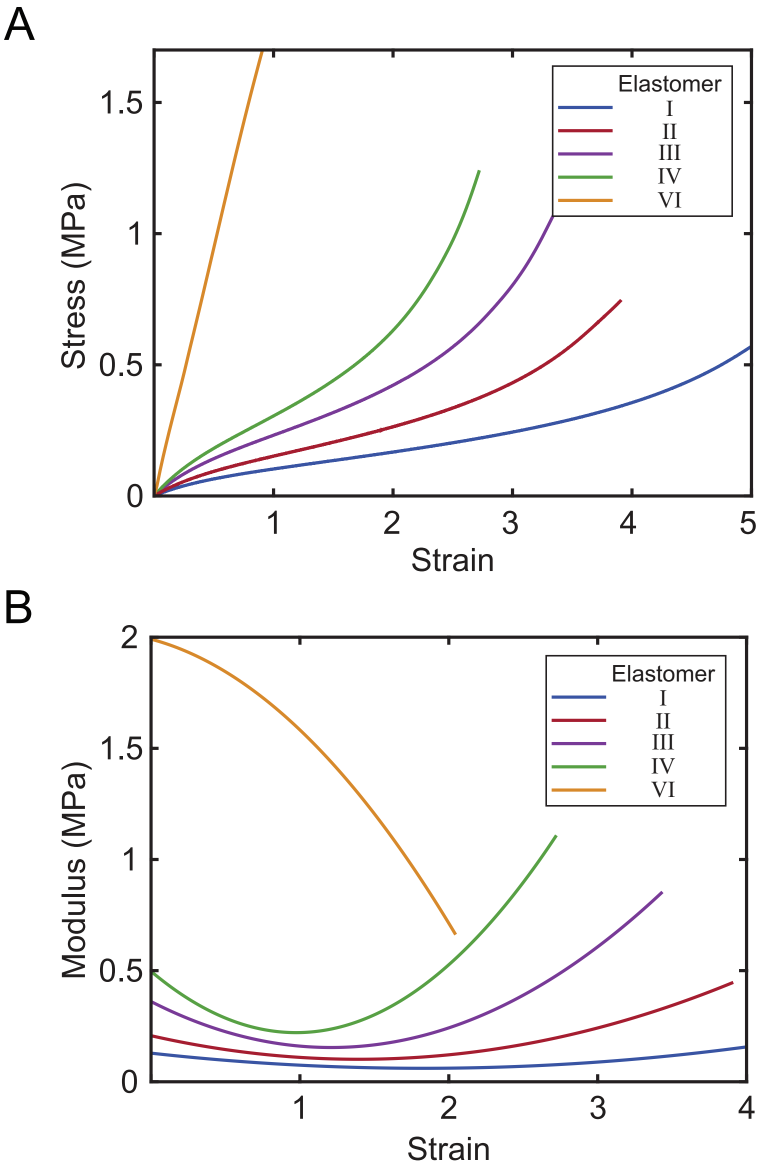

Figure 2.10: Experimentally measured (A) stress–strain and (B) elastic modulus–strain curves of the four elastomers used in the experiments.

Elastomer	Component
I	Dragon Skin$^{\text{TM}}$ 10 rubber
II	Mixture of Dragon Skin$^{\text{TM}}$ 10 and 30 rubbers with the weight ratio of 2:1
III	Mixture of Dragon Skin$^{\text{TM}}$ 10 and 30 rubbers with the weight ratio of 1:2
IV	Dragon Skin$^{\text{TM}}$ 30 rubber
V	Smooth-Sil$^{\text{TM}}$ 960 and Dragon Skin$^{\text{TM}}$ 10 rubber with the weight ratio of 1:1
VI	Smooth-Sil$^{\text{TM}}$ 960 rubber

Table 2.2: Elastomers used in the experiments.

in our experiments (Table 2.2). Just as most of elastomers used for pneu-nets, our materials are far from linear elastic. Except for elastomer VI, the moduli decrease for small strains, but eventually increase beyond the initial moduli at larger strains, which is referred to as strain hardening. We use the incompressible Gent model to express the stored strain energy density function.

Uniaxial tensile tests for elastomer III were conducted several times for the same specimen. In Fig 2.11, after the elastomer is cured, the stress-strain curve for the first time it is stretched and the fifth time it is stretched shows significant difference. The first time it is stretched, the stress-strain curve does not show significant strain-hardening effect as the yellow line shows a linear trend. Tensile test was conducted until material started to whiten showing that it has passed its yield point resulting in plastic deformation. After three times it is stretched, it converges and strain-hardening effect is shown. All experiments conducted in this paper using the strain-hardening effect were stretched at least three times before recording videos or obtaining data.

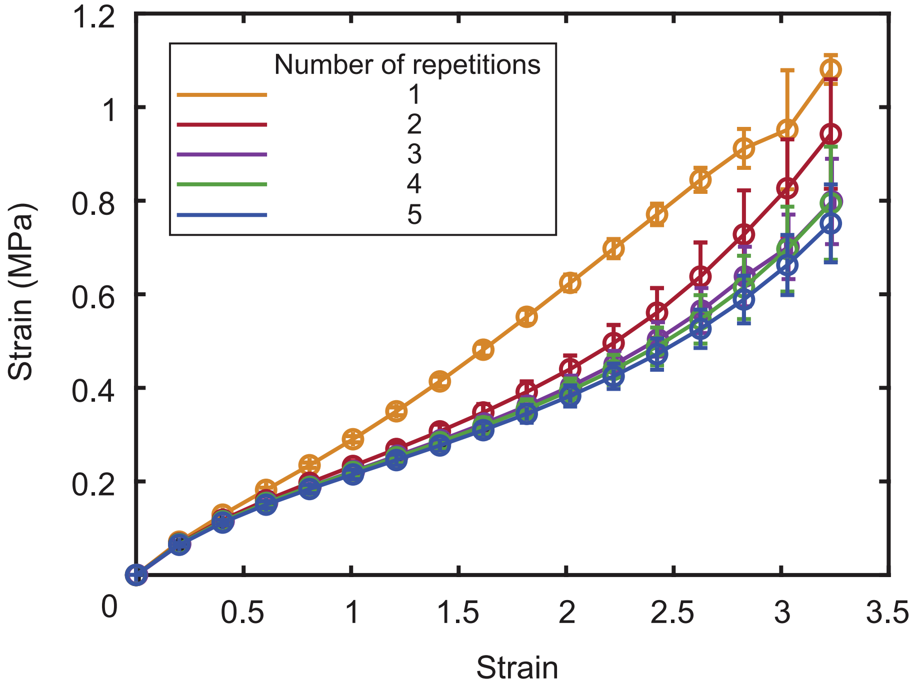

Figure 2.11: Uniaxial tensile test for elastomer III were conducted several times for the same specimen.

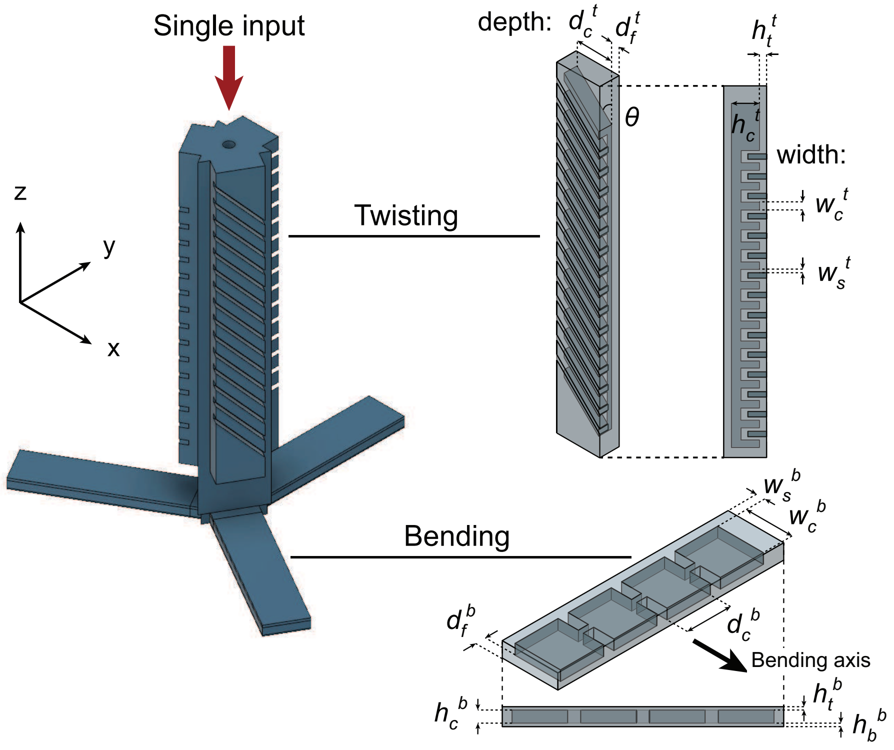

Figure 2.12: Schematics of a pneu-net system combining modules of different elastic moduli.

The theoretical results imply that we can design a pneumatic actuation device that can be deformed to a designated extent at a pre-set activation pressure by modulating the wall thickness and the elastic modulus. It is through combining multiple cells with deliberately modulated activation pressures that we achieve sequential multi-mode morphing pneu-nets, as demonstrated in the following.

2.5 Combining pneu-nets of different materials

We first present a multi-mode morphing pneu-net device that combines two sets of network modules made of elastomers with different elastic moduli, as shown in Fig. 2.12. Its upper portion has a long triangular prism-shaped shaft in the center surrounded by three identical twisting modules of pneu-net, and the lower portion consists of three identical bending modules of pneu-net. Each twisting module is a long strip with a tilted (with respect to the strip's longitudinal axis) array of air chambers which are connected to a central duct in the shaft. When pressurized, the chamber arrays in the modules swell, eventually causing the entire upper part to twist. It is because the inflation direction is perpendicular to the tilted chambers, exerting a force in both depth-wise and width-wise directions (depth-wise force induces twisting). Each twisting module and the shaft are made of elastomer III and V, respectively. Each bending module in the lower part has a linear array of thin cuboid air chambers, which is connected to the central duct. Because the bending module's bottom wall made of elastomer VI is stiffer than the other walls made of elastomer II, the pressurized air chambers bulge upward to cause each module to bend downward.

Figure 2.13A show the actuation sequence of the integrated device. When pressurized, the device begins to exhibit dominantly the bending of the lower modules, and as the pressure increases, the twisting of upper portion dominates with the lower part's bending stopped. Because all the air chambers in the device are connected to a single pressure input through the central duct, modulating the actuation pressure alone could stimulate multiple morphing modes of bending and twisting. The dimensions of the twisting and bending modules were tuned in the design stage to achieve sequential multi-mode morphing, with the aid of numerical computations. We employed a finite element analysis package, Abaqus, to predict the shape evolution of the device based on the geometric dimensions and the hyperelastic properties we measured. Figure 2.13B shows that the theoretically predicted shapes are consistent with the experimental results. Quantitative comparisons of theory and experiment are given in Fig. 2.14, which plots the curvature of the lower bending module and the rotation angle of the upper twisting module versus actuation pressure. We see that the bending curvature increases rapidly in the small pressure region ($p/\overline{\mu} < 0.44$ kPa), which

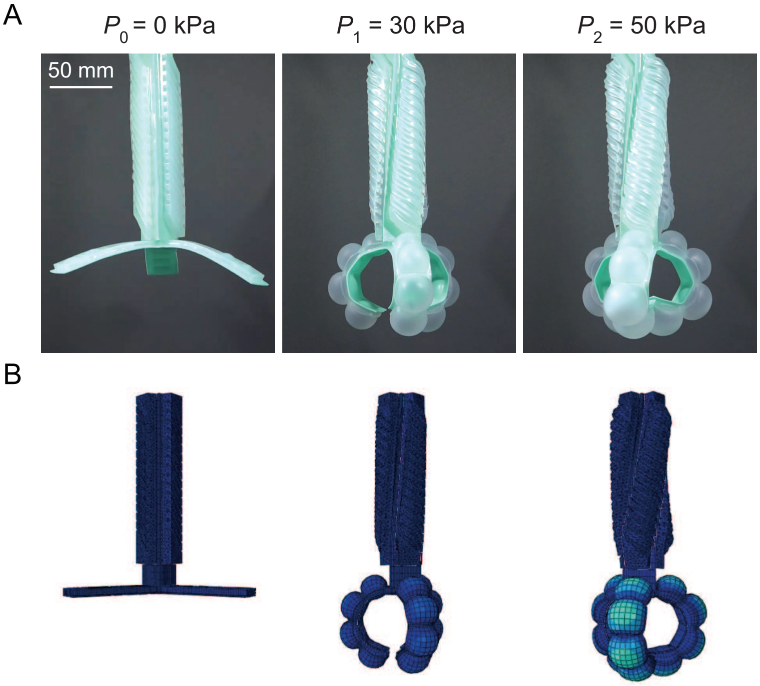

Figure 2.13: (A) Experimental images of the device undergoing sequential morphing from the undeformed initial configuration ($P_0 = 0$). As the actuation pressure increases to $P_1 = 30$ kPa, the lower modules bend with insignificant twisting of the upper shaft. As the pressure further increases to $P_2 = 50$ kPa, the upper modules twist as much as 56° from the initial state with the further bending of lower modules suppressed. (B) Numerically predicted shapes of the device at the same pressure values as (A).

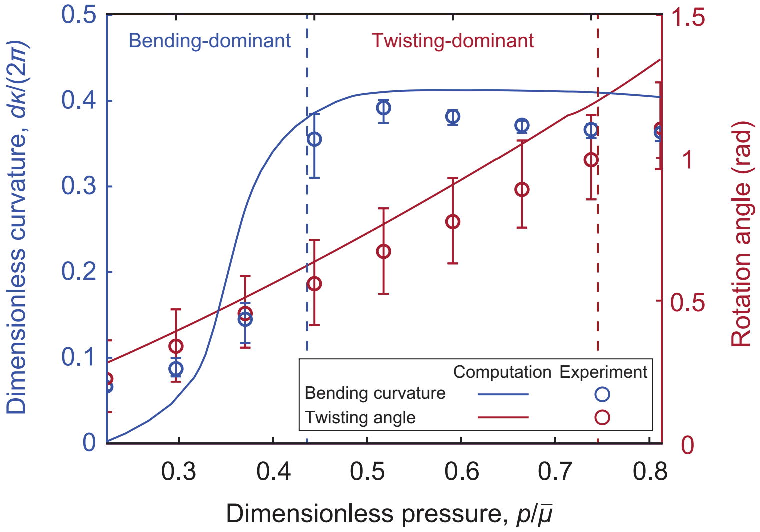

Figure 2.14: Dimensionless curvature, $d\kappa/(2\pi)$, of the lower bending module and rotation angle of the upper twisting module as a function of actuation pressure, $p/\overline{\mu}$, where $\overline{\mu}$ is the average shear modulus of elastomer II and III.

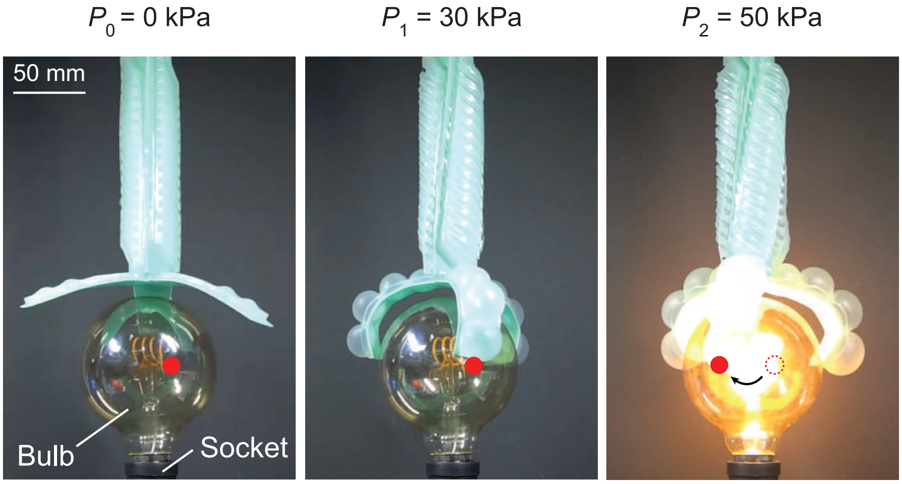

Figure 2.15: The sequential bending and twisting of the pneu-net system can turn a bulb in a socket and switch it on.

corresponds to the bending-dominant phase. In the larger pressure region ($p/\overline{\mu} > 0.44$ kPa), the bending of the lower portion is suppressed thanks to strain hardening of elastomer II while the continual twisting dominates the device morphing, corresponding to the twisting-dominant phase. Here, $\overline{\mu}$ corresponds to the average shear modulus of elastomer II and III.

Our pneu-net system capable of sequential morphing of bending and twisting can perform essential daily functions of our hands, as demonstrated in Fig. 2.15 and Fig. 2.16. Fig. 2.15 shows the bending module of the device first grips a bulb as actuated by a low pressure, and then the bulb is rotated and fit into a socket by the twisting module to be switched on at a higher actuation pressure. If the bulb is replaced by a door knob, our device can grip (by bending the lower modules) and rotate (by twisting the upper modules) the knob to open the door, as shown in Fig. 2.16. Because the pneu-net actuators are soft, the bending modules can grip a wide size range of objects of diverse shapes and excessive rotation of bulbs or knobs can be avoided. Although the multi-mode actuations of gripping and rotation of a bulb or a door knob usually require complicated mechanical elements,

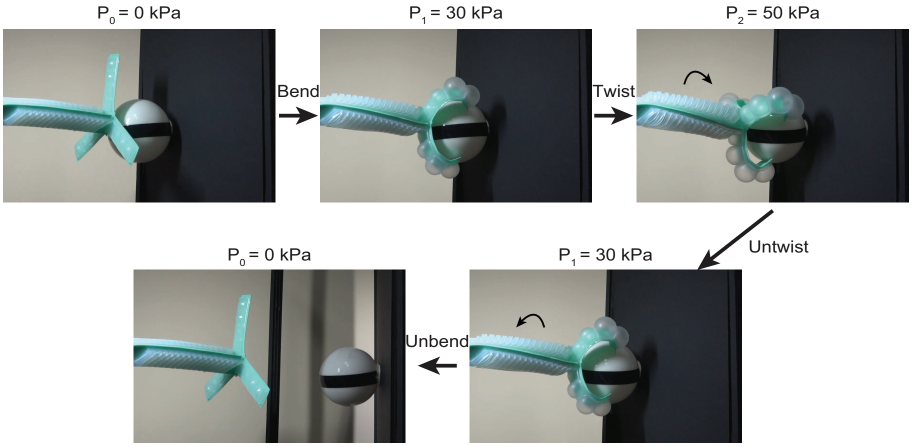

Figure 2.16: Grabbing and turning a door knob with our sequential multi-mode morphing actuation system. Sequential releasing of the pneu-net system shows the reversal process to untwist, then unbend.

electronic circuits, and sophisticated control inputs in conventional rigid robots, our simple pneu-net system made of elastomers can perform the similar multiple tasks using only a single pressure input.

Although we have shown that our actuator can be used to grab and turn on a light bulb or open a door through sequential activation of different segments, we have not conducted force measurements or cyclic tests as our research aims to utilize the strain-hardening effect to create different morphologies at distinct pressures. We focused on taking measurements that show the change in morphology by measuring the curvature, rotation angle, and stretching distance as pressure is increased. We wanted to show potential applications using our approach, but put our main focus on proposing an alternative method to morph more than once using a single-input device. The following sections showing different types of sequential morphing are all focused in showing sequential morphing, rather than putting focus on the applications which is why there are no force measurements.

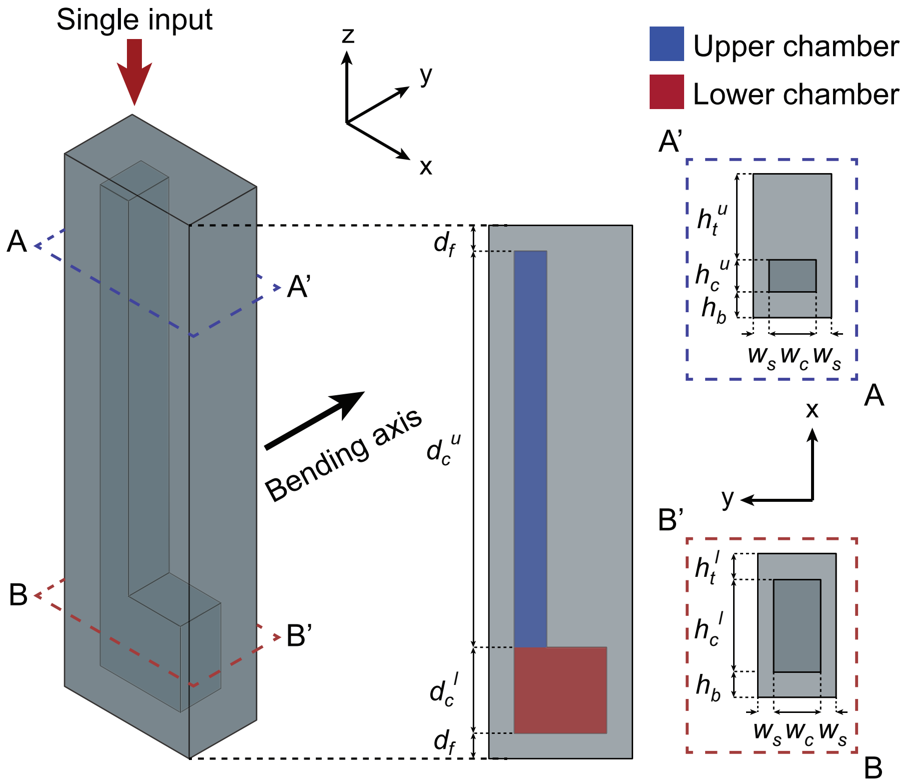

Figure 2.17: Schematics of a pneu-net system with contrast in wall thickness.

2.6 Combining pneu-nets of different thicknesses

We can confer contrast in stiffness on a pneu-net system by giving each chamber different wall thickness. We show such a device, which is capable of sequential stretching–bending, in Fig. 2.17. Its schematic is shown in Fig. 2.17, where a cuboid made entirely of elastomer III houses a long slender upper chamber connected to a wide lower chamber. Although the chambers have the identical side wall thickness w_s and the bottom height h_b, the difference in top wall height (h_t^u and h_t^l) allows us to attain sequential multi-mode morphing. Figure 2.18A shows the experimental images of the device actuated at different pressure through a single pressure input source. Because the lower chamber has a smaller wall height h_t^l than the upper chamber's wall height h_t^u, the deformation of the lower chamber – stretching in the y-direction in this case – is dominant in the lower pressure conditions (P_1 = 120 kPa). As the pressure exceeds the critical pressure to induce the significant bending of the upper chamber with a thick top wall, the device with the lower chamber already bulged is now bent at the upper stalk, as shown in Fig. 2.18A at P_2 = 150 kPa.

Figure 2.18B shows that the device shapes numerically predicted by the finite element analysis are consistent with the experimental results. Quantitative comparison of the experimental and computational results is made in Fig. 2.19, where the stretch of the lower chamber and the bending curvature of the upper chamber are plotted versus the actuation pressure. In addition to the agreement of theory and experiment, we see that the critical pressure values for the rapid rise of the upper chamber's bending curvature and for the strain hardening of the lower chamber coincide ($p/\mu = 0.49$), a result of our deliberate design through iterative simulations with changing parameters. By matching the critical pressure values, the stretching-dominant regime smoothly transitions to the bending-dominant regime as the critical pressure is crossed over.

Combining pneu-nets of different thicknesses can be used to make a self-standing crawling soft robot. Conventional crawling soft robots are capable of linear locomotion through repetitions of inflation and deflation. However, they are not capable of reorienting their positions if pushed to stand on their sides. A self-standing crawling pneu-net shown in Fig. 2.20A is designed using stretching to push a crawling pneu-net to stand upright at a moderate positive pressure P_1 of 110 kPa, then proceed to crawl forwards through repetitions of deflation to P_0 and P_2 at 140 kPa. A multi-functional soft crawling robot can be designed as such to increase the complexity in terms of functionality without having to use numerous input tubes which would make it harder to control and actuate properly.

Another application can be to perform sequential stretching and bending to hold, seal and move a jar, as demonstrated in Fig. 2.20B. At zero

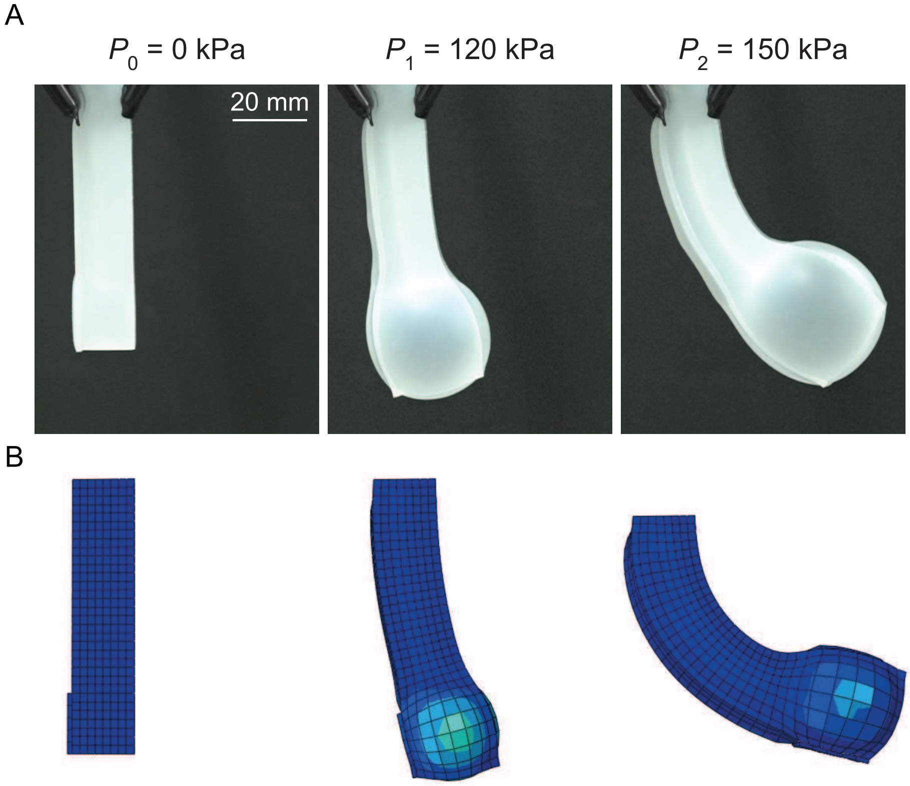

Figure 2.18: (A) Experimental images of the device undergoing sequential morphing from the undeformed initial configuration ($P_0 = 0$). As the actuation pressure increases to $P_1 = 120$ kPa, the lower chamber is bulged with insignificant bending of the upper chamber. As the pressure further increases to $P_2 = 150$ kPa, the upper chamber bends with the further bulging of the lower chamber suppressed. (B) Numerically predicted shapes of the device at the same pressure values as (A).

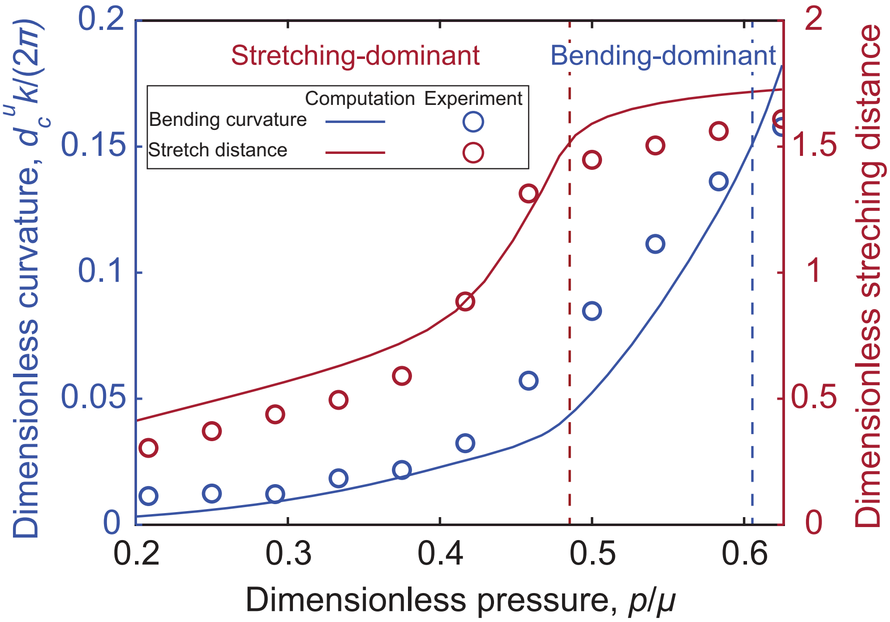

Figure 2.19: Amount of stretching and bending of the lower and upper chamber, respectively, as a function of the actuation pressure. Here, $\mu = 80$ kPa is the shear modulus of elastomer III.

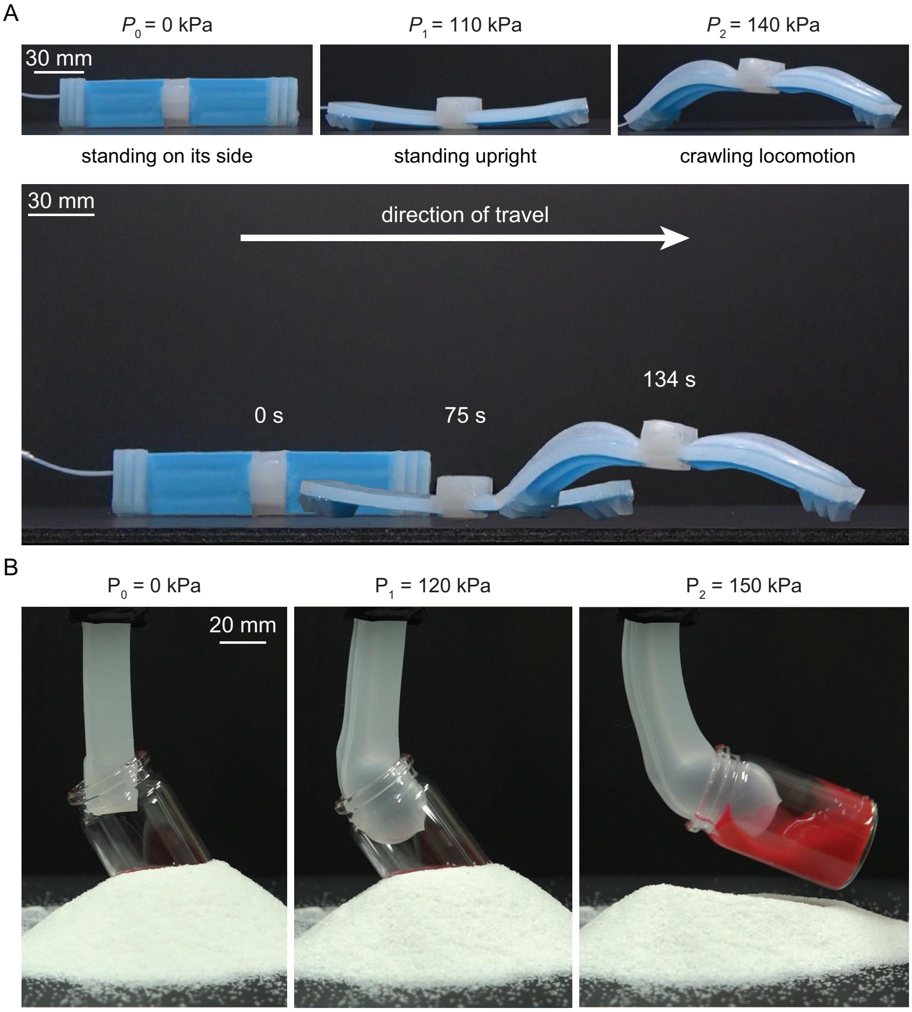

Figure 2.20: (A) A self-standing crawling pneu-net can stand upright by pushing itself, then crawl forwards. (B) A pneu-net system first holds a jar by bulging in the lower part, and then lifts it out of a sand pile without spilling by bending in the upper stalk.

activation pressure, the slender device is inserted in the opening of a jar. Then the device is inflated near its end to seal and hold the jar from inside at the activation pressure P_1 = 120 kPa ($p/\mu = 0.49$). Increasing the pressure to P_2 = 150 kPa ($p/\mu = 0.61$) bends the device to pull the jar off the unwanted environment without spilling the inner content owing to the seal provided by the inflated pneu-net body. A self-standing crawling pneu-net can also be designed to stand upright using stretching, to crawl forwards by bending.

2.7 Combining pneu-nets of different air chamber geometries

Here we demonstrate a pneu-net system having different air chamber geometries within a device to achieve multiple bending curvatures depending on the activation pressure from a single-input source. Figure 2.21 shows a schematic of the device, a long cuboid housing three chambers – slender upper and lower chambers connected by a middle chamber consisting of three relatively wide sub-chambers. The entire pneu-net was made of elastomer III except the bottom wall of the middle chamber made of stiffer elastomer VI. Because wide chambers with a smaller side wall thickness w_s^m can bulge more easily than narrow chambers with a larger side wall thickness w_s^l, the middle chamber is activated earlier than the upper and lower chambers. Experimental images in Fig. 2.22A show that the initially straight device at P = 0 morphs into a C-shape due to the bending of the middle chamber until the activation pressure reaches P_1 = 105 kPa. The free end of the device is pointing to the right. Further increase in the pressure causes the upper and lower chambers to bend in the sense opposite to the middle chamber's, making the free end point to the left, as shown in the panel corresponding to P = 130 kPa.

The pneu-net shapes predicted by numerical computation, shown in Fig. 2.22B, are consistent with the experimental images. Figure 2.23 quan-

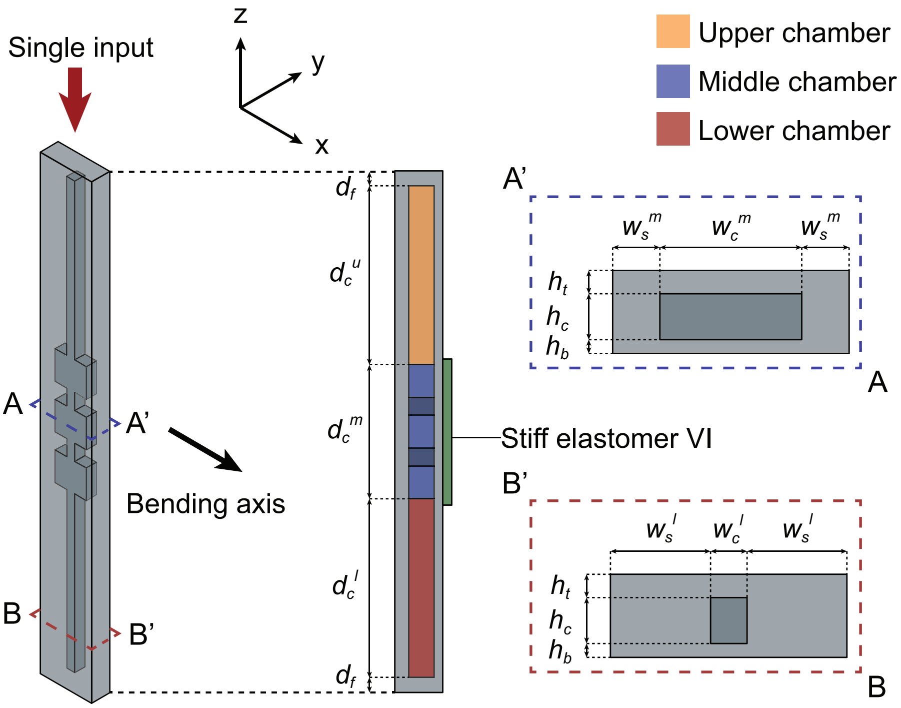

Figure 2.21: Schematics of a pneu-net system having a smaller side wall thickness in the middle than the upper and lower chambers.

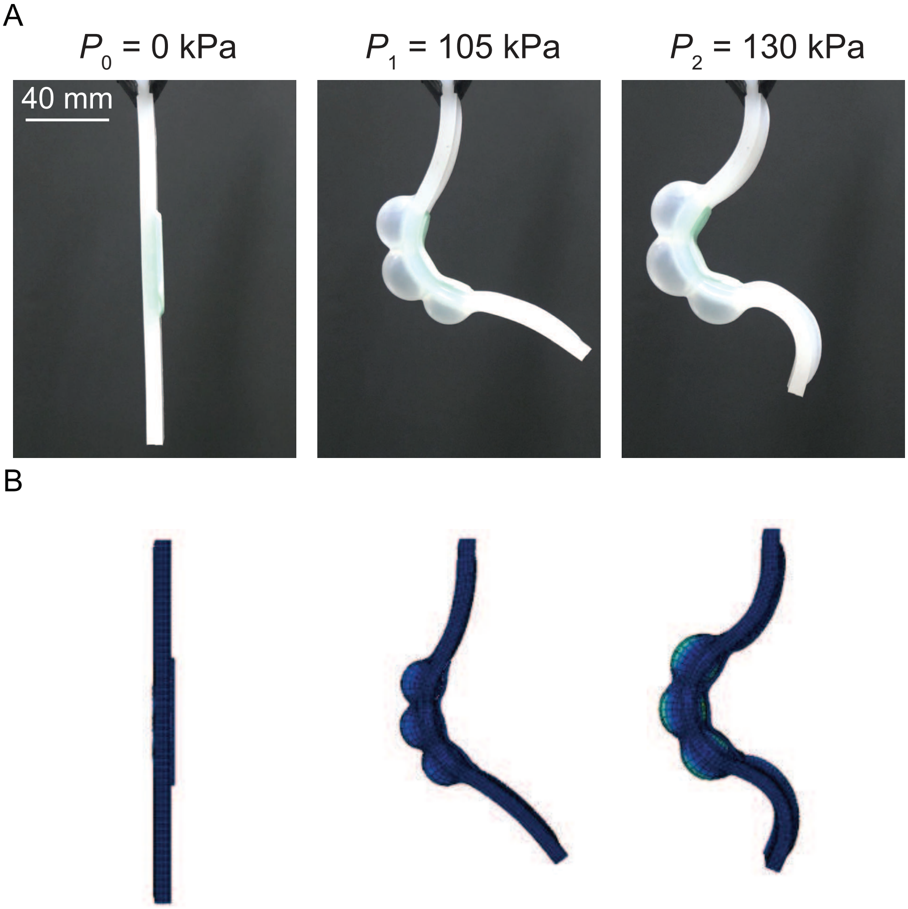

Figure 2.22: (A) Experimental images of the device developing multiple curvatures as the activation pressure increases. (B) Numerically predicted shapes of the device at the same pressure values as (A).

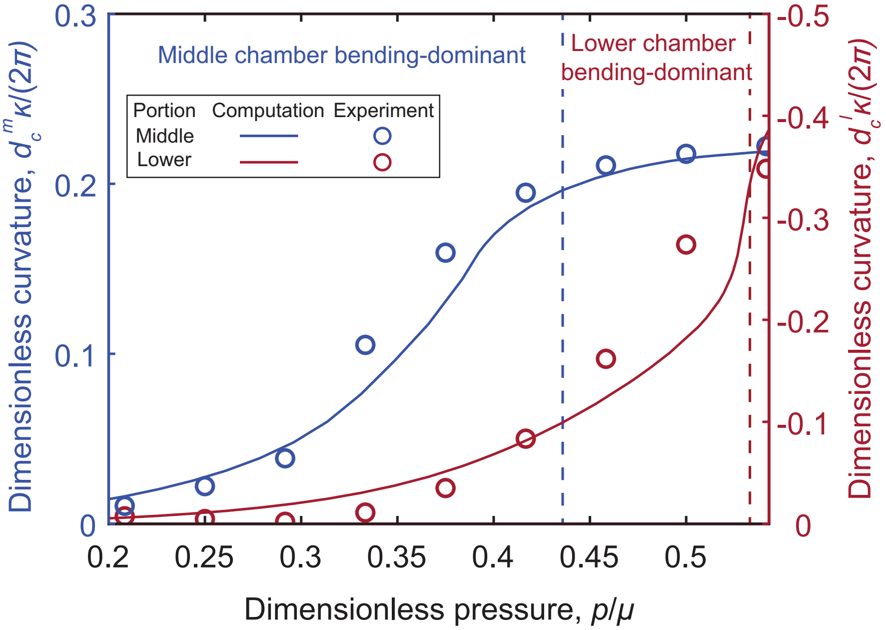

Figure 2.23: The curvatures of middle and lower chambers versus the actuation pressure.

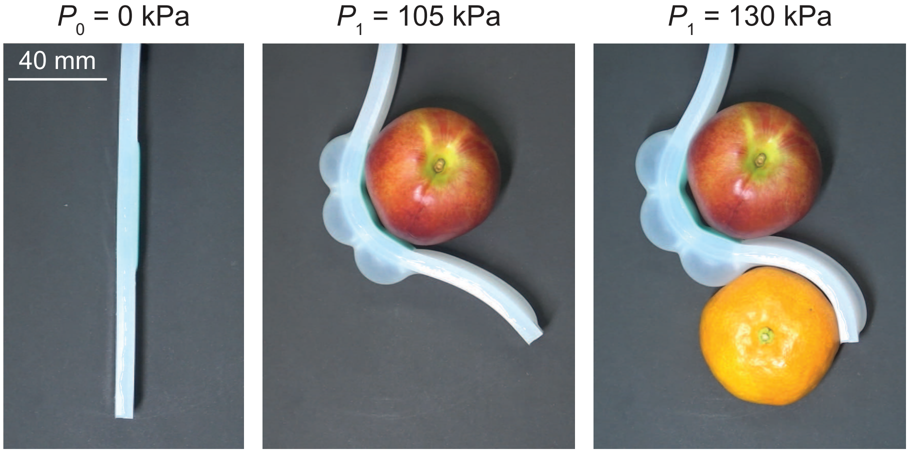

Figure 2.24: A pneu-net system grasps a red peach with bending of the middle chamber (P = 105 kPa), and then an orange with bending of the lower chamber at an increased pressure (P = 130 kPa).

titatively compare the experimental and computational results of the curvatures of middle and lower chambers versus the dimensionless actuation pressure, p/μ. Here, μ corresponds to the shear modulus of elastomer III. While the curvature increase of the middle chamber is dominant in the low pressure regime ($P < P_1$), the middle chamber's curvature is saturated when $P > P_1$ owing to strain hardening. But in the high pressure regime, the curvature of the lower chamber (also that of the upper chamber) steeply increases with the pressure. The smooth transition from the middle chamber bending dominant regime to the upper and lower chamber bending dominant regime is a result of our deliberate design to match the pressure values (P_1) of middle chamber's strain hardening and of rapid rise of the other parts' bending, through iterative simulations.

Multiple curves achieved by a single pneu-net can be utilized to grasp multiple objects, as demonstrated in Fig. 2.24. While the middle chamber grasps a red peach at a low actuation pressure, increasing the pressure allows the pneu-net to grasp another object, an orange, with its lower chamber's curvature. Such multiple-object grasping by forming multiple curves at different activation pressures is controlled by a single pressure input.

2.8 Conclusions

We have fabricated an actuator that can sequentially multi-mode morph using a single pressure input based on a pneumatic network that can bend, stretch or twist. Our actuator used the strain-hardening effect of elastomers as a stopping mechanism to prevent over-expansion of the softer part within our pneu-net system, which is tuned to arise at the activation of the stiffer part. Using the actuators, we designed multiple high degree-of-freedom soft devices that only rely on a single input to perform complex tasks. Although we used a pneumatic stimulus and elastomer-based actuators, single-input multi-mode morphing can be implemented in other soft robotic systems. Hydrogels, for example, also display strain-hardening behavior (Cui *et al.*, 2014; Huang *et al.*, 2017), allowing the design of single-input multi-mode morphing soft robots that use stimuli not limited to air pressure. We further proposed a theoretical model of the actuator which provides a design framework for utilizing the strain-hardening effect in multi-mode morphing soft robots.

Strain-hardening can also serve as a tool to encode physical intelligence in existing soft robotic systems. Conventional methods of increasing deformation modes and functions have relied on increasing the number of external stimuli (extra pumps, more valves, etc.) (Huang *et al.*, 2017; Shah *et al.*, 2021) or changing the environment (e.g., magnetic, electric, humidity) (Dong *et al.*, 2022; Vasios *et al.*, 2020), leading to higher costs and control complexity. By exploiting the strain-hardening effect, higher functionality can be easily achieved, suggesting a new paradigm for soft robotic design and control.

Chapter 3

Multi-mode morphing of pneumatic actuators using phase transition

Multi-mode morphing using pneumatic actuators using only a single input have been shown to be possible using the inherent property of strain-hardening of elastomers in the previous chapter. In this chapter, we achieve multi-mode morphing of pneumatic actuators using liquid-solid phase transition through an embedded stiffness programmable layer (SPL). We show that by controlling temperature of specific regions of a pneu-net device, we can locally control the stiffness without having to add additional inputs. This approach is not limited to dual morphing, but is reprogrammable which enables the device to morph numerous times. Using our theoretical model, we show how states of matter inside the SPL affects the effective stiffness within a pneumatic device that can be used to control the stiffness. We also show various applications such as multi-mode morphing of a cylindrical pneumatic device, and interacting with the environment to create a pixelated morphing system.

We used the strain-hardening effect of elastomers in the previous chapter to achieve multi-mode morphing which can be implemented into any pneumatic device. In contrast, rather than using the material properties of elastomers to achieve multi-mode morphing, we add another layer to control stiffness that does not need additional inputs. We use temperature as an additional stimulus to control stiffness which can easily be achieved using our environment. For example, human touch can provide sufficient heat in a cold environment which can create local heating. This enables the device to deform more than twice, and gives it a huge advantage of being reprogrammable despite being a pneu-net.

In §3.1, we provide a brief introduction to our research. Then, using a trilayer beam, we control the onset of morphing by modulating stiffness depending on the state of matter inside the SPL layer in §3.2. In §3.3, we experimentally show an SPL embedded pneu-net unit cell and how it deforms when there is a gas, liquid, or solid present inside the SPL. Using a capillary burst valve, we show multi-mode morphing depending on the surface tension of liquids in §3.4. Using our findings, we show how a multi-mode morphing cylindrical pneu-net device with embedded semicircular SPL chambers can be made in §3.5. Then in §3.6, we show a reprogrammable pixelated multi-mode morphing device capable of interacting with the environment to change its morphology when actuated. Finally, we summarize our study in §3.7.

3.1 Introduction

Multi-mode morphing soft actuators have been introduced in various ways to perform various tasks. Single morphing actuators can only conduct simple tasks, whereas multi-mode morphing actuators can conduct more than one task, or perform more complicated tasks. This has been conducted through various means such as modulating local stiffness through dielectric elastomers (Aksoy & Shea, 2020), using origami (Kim *et al.*, 2019; Li & Wang, 2015), or using acoustics (Aghakhani *et al.*, 2020; Kaynak *et al.*, 2020). The applications of soft actuators have been used as soft grippers

(Tawk *et al.*, 2019; Wang *et al.*, 2020; Zhou *et al.*, 2021), artificial muscles (Mu *et al.*, 2019; Yuan *et al.*, 2019), haptics (Kanjanapas *et al.*, 2019; Thai *et al.*, 2020), and biomedical devices (Kashyap *et al.*, 2020; Payne *et al.*, 2017). We focus on pneumatic actuation for its rapid actuation. For multi-mode morphing pneu-nets, numerous input pipes have been used to control each pneu-net separately in the form of pixels (Hu *et al.*, 2022). Although this enables a complex pneumatic system to morph with high degree of freedom, it requires a complex system to control each pneu-net separately which makes it hard to control and manufacture.

Here we present a pneu-net device with an embedded stiffness programmable layer (SPL) to achieve multi-mode morphing using phase transition. Using only a single pneumatic source, our device is capable of reprogramming to morph into numerous different shapes which is unconventional for pneu-nets. By adding a void network within the top wall of a conventional pneu-net, we can control the effective stiffness of different regions within a single pneu-net to create different morphologies upon actuation. We first fill the SPLs with either gas (air), liquid (water) or solid (ice). Using the property of fluids being incapable of contributing stiffness while solids can, we use liquid-solid phase transition of water and ice to alter effective stiffness. Using a temperature controlled chamber to freeze the water inside SPL chambers, we use external heat to melt the ice in specific regions of SPL chambers while keeping all others frozen. When inflating the pneumatic layer, the softer part of the pneu-net device (where water fills the SPL chamber) will deform prior to the stiffer part (where ice fills the SPL chamber). Thus, we can control local stiffness without having to change the pneu-net design or using multiple pneumatic sources to control individual chambers.

Regarding the practicality of the pneu-net with an embedded layer, if left at room temperature, all the ice inside the SPL chamber would melt. Our pneu-net device with an embedded SPL is fit to function in cold environments due to our selection of liquid which is water. Our goal is to propose a simple method to modulate stiffness which was why we used water, which is a ubiquitous liquid, through a SPL which can respond to environmental stimulus (heat). However, replacing the liquid with a liquid metal (Wang *et al.*, 2021a), can be used to actuate the device at room temperature. Using body heat at body temperature, transitional ferrofluids can be designed to melt with human touch, then solidify at room temperature to undergo phase transition fit for room temperature.

To explain further on why water was chosen as our liquid to fill the SPL chambers, water is an abundant, inexpensive resource that can phase transition from liquid to solid near 0 °C. We wanted to propose a simple method to modulate stiffness using a ubiquitous liquid, rather than using an expensive, complicated method to achieve the same results. We eliminated the use of liquids that silicone elastomers absorb well, and liquids that are harmful to humans as they cannot be used as tangible displays and haptics. Liquid metal can be useful to lower the melting point of the solid, but are very expensive and cannot be interchanged due to the adhesion and contamination to the elastomer. If we observe the swelling ratio of polydimethylsiloxane (PMDS) elastomer by weight and volume for different liquids shown in Fig. 3.1 (Rumens *et al.*, 2015), we can see a lot of organic solvents are absorbed. Excluding the dangerous liquids, we can use liquids such as ethanol that are relatively safe to use with low swelling ratios. Although this graph shows the swelling ratio for PDMS, the elastomer used in our pneu-nets have similar swelling ratios as they are both silicone-based elastomers.

In the following, we first explain the mechanical model for effective stiffness using a trilayer beam, which forms the basis of stiffness control via phase transition. We then demonstrate a simple unit cell with an embedded SPL to show that stiffness can be controlled depending on the state of matter inside the SPL. Using a capillary burst valve and properties of different liquids, we show multi-mode morphing depending on the liquid filled in the SPL chambers. We design and demonstrate a multi-mode morphing pneu-net which can bend to opposite curvatures, stretch or morph into different

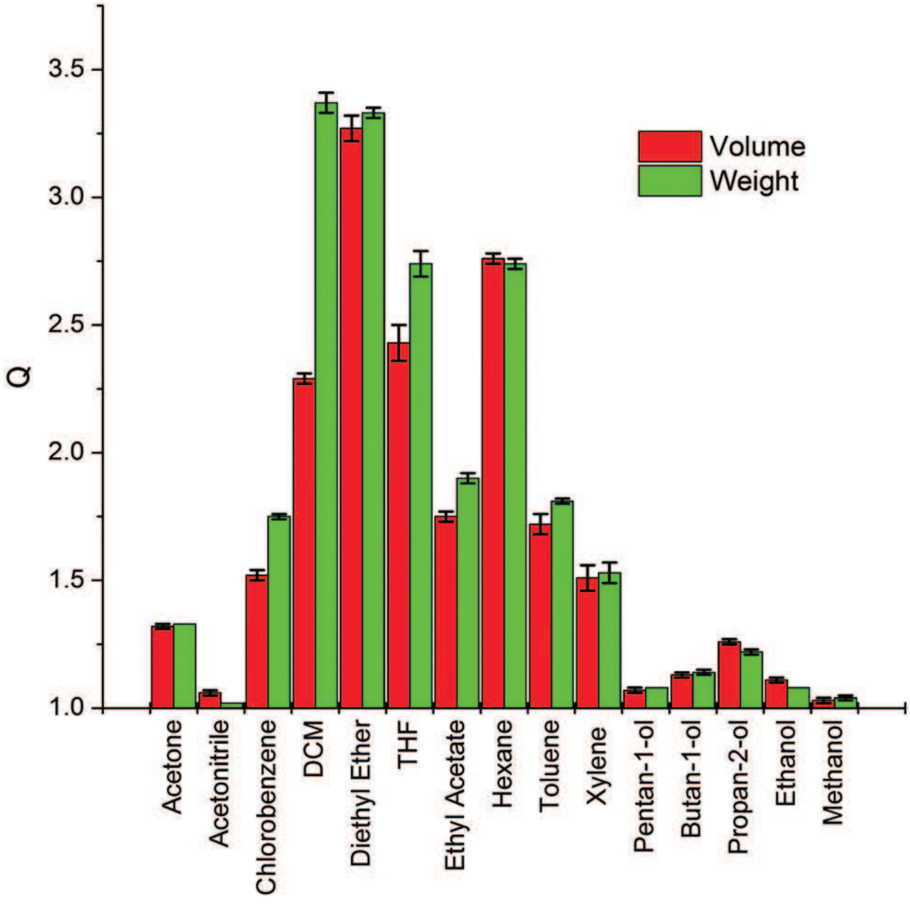

Figure 3.1: Swelling ratio of PDMS elastomer by weight and volume for different liquids. Image adapted from (Rumens *et al.*, 2015).

shapes. Finally, we show a reprogrammable pixelated multi-mode morphing device capable of interacting with the environment to freely 'draw' any morph into any design. We show that these multi-mode morphing pneu-net schemes enable a single device to morph numerous times with a single pneumatic source.

Since our pneu-net with an embedded SPL uses heat to modulate stiffness of wanted pixels, infrared imaging of the pixelated pneu-net could be used to show actuation (Hwang *et al.*, 2022; Lee *et al.*, 2019). Infrared imaging is commonly used to show the temperature change as the actuated parts responding to heat can change shape with temperature. Our device uses external heat source which changes the phase state of water and ice which will show similar results to previous research using infrared imaging, but we decided to focus only on the shape change of our device rather than showing the temperature change of specific cells. Additionally, since our device focuses on using external heat rather than embedding a heating element such as the ones introduced (Hwang *et al.*, 2022; Lee *et al.*, 2019), we only show experimental images using a normal camcorder instead of an infrared camera.

3.2 Mechanical model

Using a simple model to describe how we control the onset of morphing by modulating stiffness (determined by elastic modulus and thickness), we consider a trilayer beam with top and bottom layers of constant thickness and modulus h_1, and E_1 that can bend about the neutral axis, as shown in Fig. 3.2. We can model the trilayer beam and corresponding single layer beam as they should be identically stretched under the same tensile load. The effective Young's modulus and thickness can be expressed as

$$\overline{Eh} = 2E_1h_1 + E_2h_2. \tag{3.1}$$

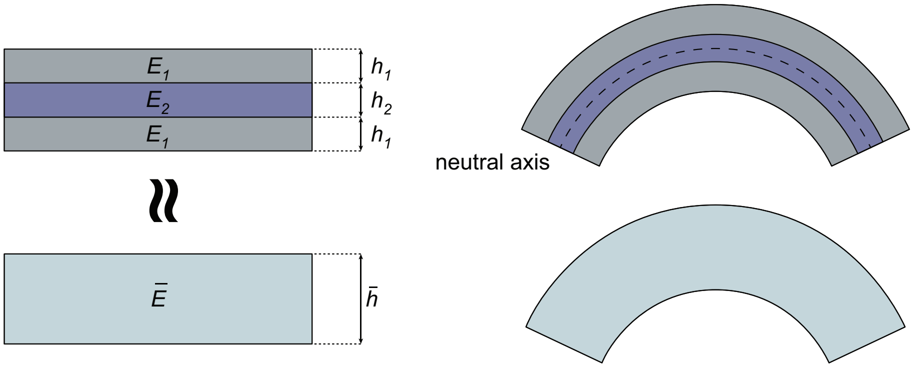

Figure 3.2: Schematics of trilayer beam and its corresponding single layer beam.

where $\overline{E}$ and $\overline{h}$ correspond to the effective Young's modulus and thickness, respectively. The bending stiffness can then be derived as

$$\overline{K} = \frac{2}{3}E_1[(h_1 + \frac{1}{2}h_2)^3 - \frac{1}{8}h_2^3] + \frac{1}{12}E_2h_2^3 = \frac{\overline{E}\,\overline{h}^3}{12}, \tag{3.2}$$

where $\overline{K}$ is the effective bending stiffness of the corresponding single layer beam. Rearranging equation 3.2 to make $\overline{h}$ the subject, we can obtain a relationship for effective thickness as

$$\overline{h} = \left[\frac{E_1(8h_1^3 + 12h_1^2h_2 + 6h_1h_2^2) + E_2h_2^3}{2E_1h_1 + E_2h_2}\right]^{\frac{1}{3}}. \tag{3.3}$$

Substituting equation 3.3 into 3.1, we can finally obtain the effective stiffness $\overline{E}$, of a trilayer beam.

We compute the effective stiffness as a function of dimensionless thickness, expressed as the thickness of middle layer h_2 over total thickness h, for three different materials in the middle layer. Figure 3.3 shows the results for fluid, Ecoflex 30, and ice put in the middle layer. For a fluid filled in the middle layer, the Young's modulus E_2 is set as 0 as fluids cannot resist shear (White, 1991), leading to low relative stiffness that is independent of middle layer thickness. Ice has a Young's modulus in the scale of 10^{10} Pa (Butkovich, 1959), resulting in an extremely high effective stiffness

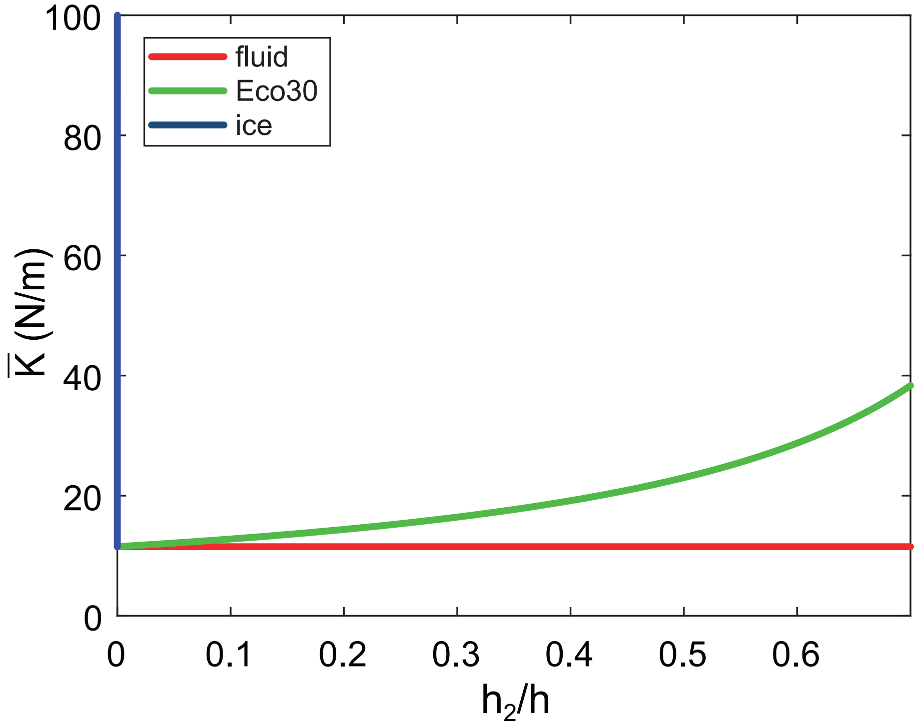

Figure 3.3: Effective stiffness as a function of dimensionless thickness (expressed as thickness of middle layer over total thickness) for three different materials put in the middle layer.

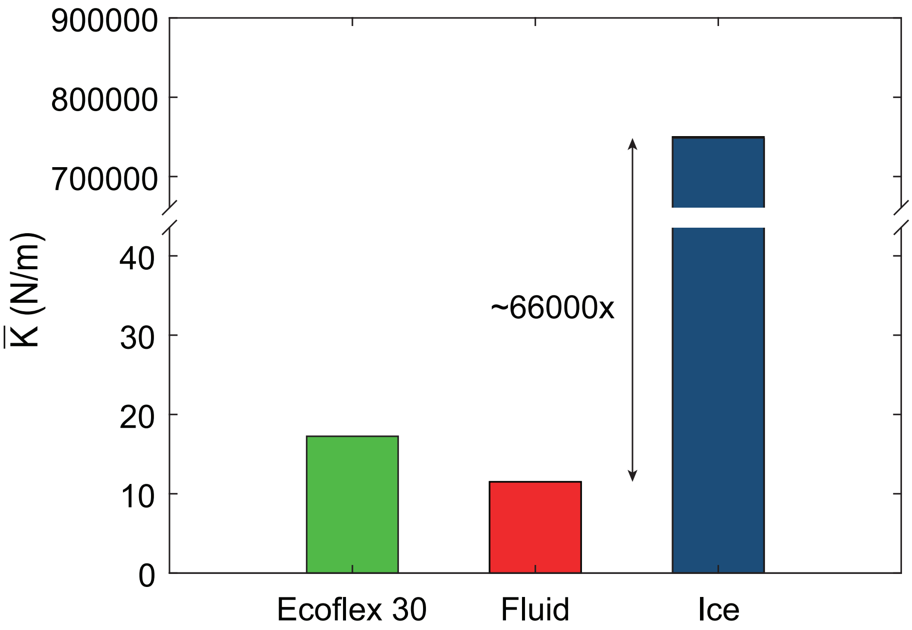

Figure 3.4: Effective stiffness when Ecoflex 30, fluid, and ice is put in the middle layer for $h_2 = 1$ mm. The difference in effective stiffness is approximately 66000 times between fluid and ice.

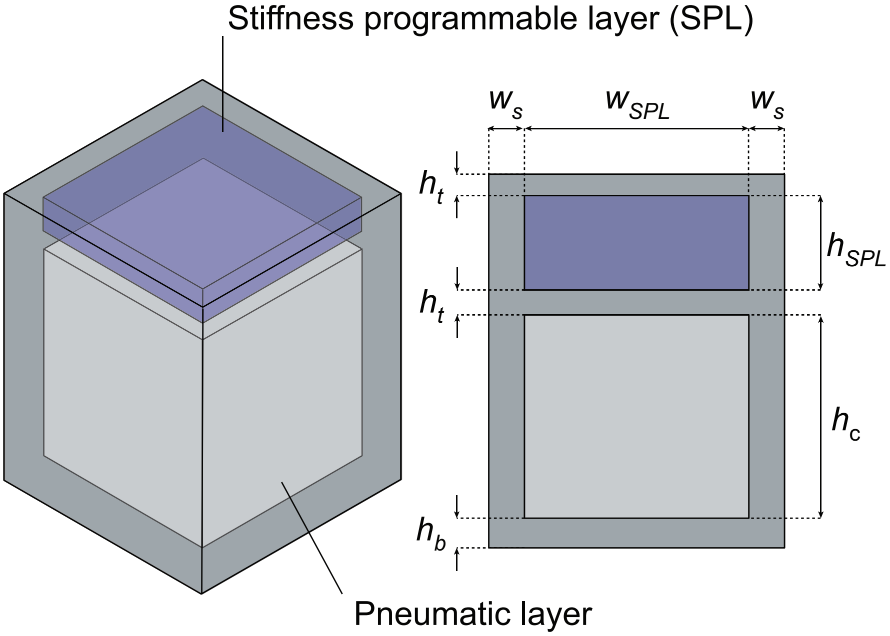

Figure 3.5: Schematics of a pneumatic unit cell with an embedded stiffness programmable layer (SPL).

that is approximately 66,000 times greater than that filled with a fluid as shown in Fig. 3.4. Therefore, if two trilayer structures containing a fluid and ice in its middle layer are subject to the same load, the one containing fluid would deform first. Although it is obvious that a solid provides more stiffness than a fluid, Fig. 3.4 confirms these results.

The theoretical results imply that we can design a pneumatic actuation device with an embedded stiffness programmable layer in the form of a trilayer with fluid or solid to control deformation morphology.

3.3 SPL embedded pneu-net unit cell

We present a multi-mode morphing pneu-net device with an embedded stiffness programmable layer (SPL), as shown in Fig. 3.5. The pneu-net is made of Ecoflex 30 with a pneumatic layer to activate the soft actuator,

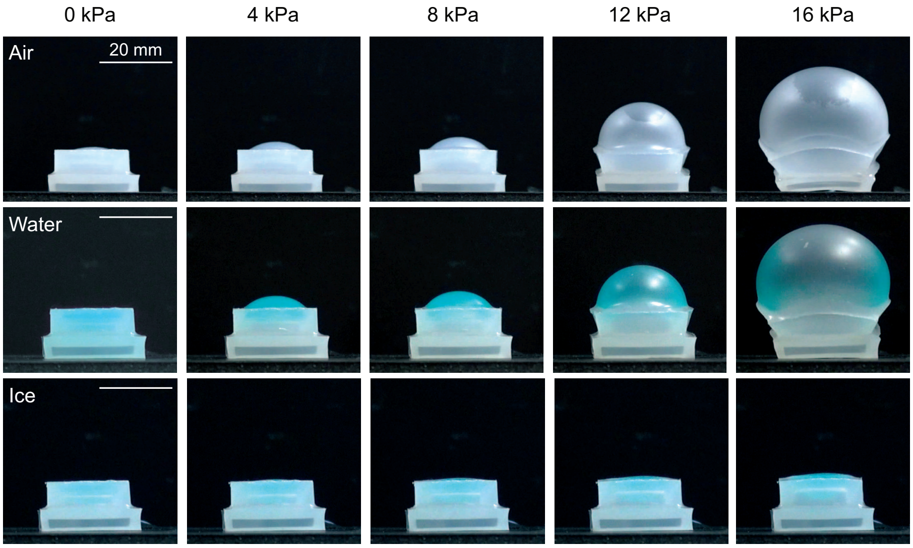

Figure 3.6: Experimental results of air, water, and ice filled in the SPL layer for $h_{SPL} = 1.5$ mm, as pressure increases.

and a SPL layer with either air, water, or ice by freezing the water at -10 °C inside a temperature controlled chamber. Depending on whether a fluid or solid is filled inside the SPL layer, the stiffness of the pneu-net device can be controlled as shown in Fig. 3.3.

Fig. 3.6 shows the actuation sequence of the unit cell. When pressurized, for unit cells with air and water encapsulated in the SPL layer, they deform immediately for small pressure, and continue to inflate further as pressure is increased to 16 kPa. For ice inside the SPL layer, due to its extremely high effective stiffness, it hardly inflates at the same pressure. All geometrical parameters shown in Fig. 3.5 are kept constant for all three experiments.

Quantitative analysis of the deformation behavior of unit cells of varying SPL layer thickness are shown in Fig. 3.7. All other geometrical parameters were kept constant. For various SPL layer thickness, h_{SPL}, we observe air and water showing similar results, initially deforming mildly as pressure is increased, then due to classical instability of top walls (Gent, 1996) at approximately 10 kPa, deformation is increased greatly. Ice, on the other

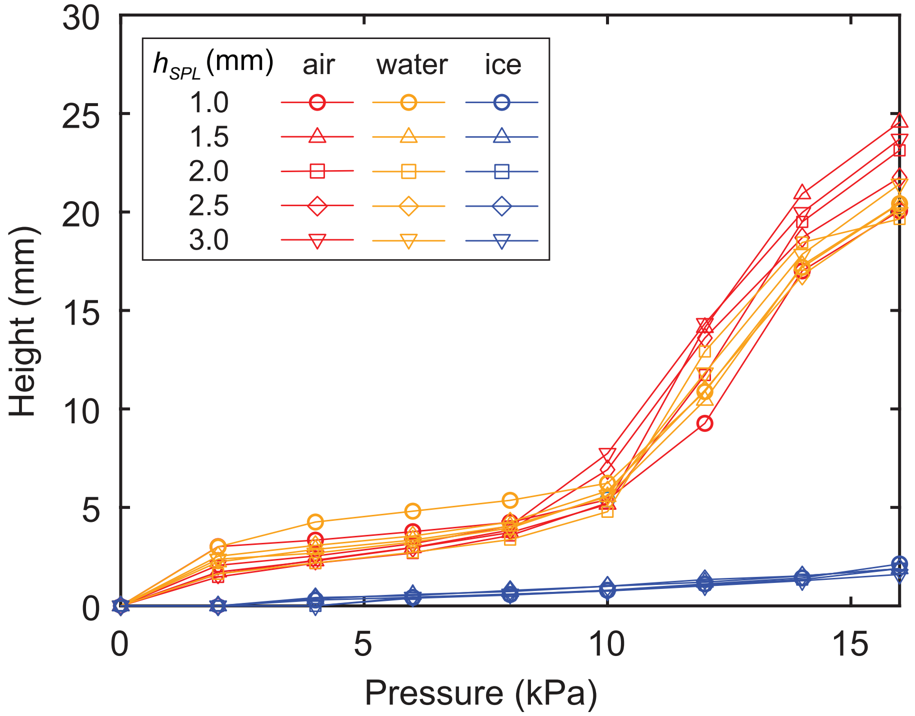

Figure 3.7: Deformation (height) versus pressure for different SPL thickness, h_{SPL}, for air, water and ice.

hand, hardly shows any deformation as pressure is increased due to its significantly high effective stiffness as shown in Fig. 3.3. We find that SPL layer thickness is not an important factor in determining deformation, owing to the drastic difference in Young's modulus and effective stiffness of fluids and solids.

Using our findings that effective stiffness modulated using different states of matter inside the SPL, we can combine multiple cells with deliberately modulated effective stiffness to achieve reprogrammable multi-mode morphing pneu-nets. In the following chapters, we use a capillary burst valve to multi-mode morph depending on the surface tension of liquid use in the SPL. Them, we introduce two different types of multi-mode morphing pneu-nets using water. First, we design a cylindrical pneu-net to melt specific SPL chambers to exhibit different morphologies. By melting all SPL chambers and freezing it, it will return to its original state where all SPL chambers are frozen. This makes it reprogrammable despite being a pneu-net. Similarly, in §3.6, we introduce a pixelated pneu-net capable of interacting with the environment through heat.

3.4 Multi-mode morphing using SPL and capillary burst valves

In this section, we integrate a capillary burst valve into our pneu-net system to fully utilize the property of liquids. Surface tension is a property only liquids have which can be used to control channel design by using it with a capillary burst valve (Cho *et al.*, 2007). We used the following three liquids to achieve different designs: water, ethanol (11%), and acetic acid (10%). The reason behind using these specific liquids in the concentrations specified above has to do with how a capillary burst valve functions.

We design our SPL in the design shown in Fig. 3.8A, where the locations of valve 1 and 2 determine how far a specific liquid is able to fill. Due to the difference in surface tension of water, ethanol, acetic acid, their

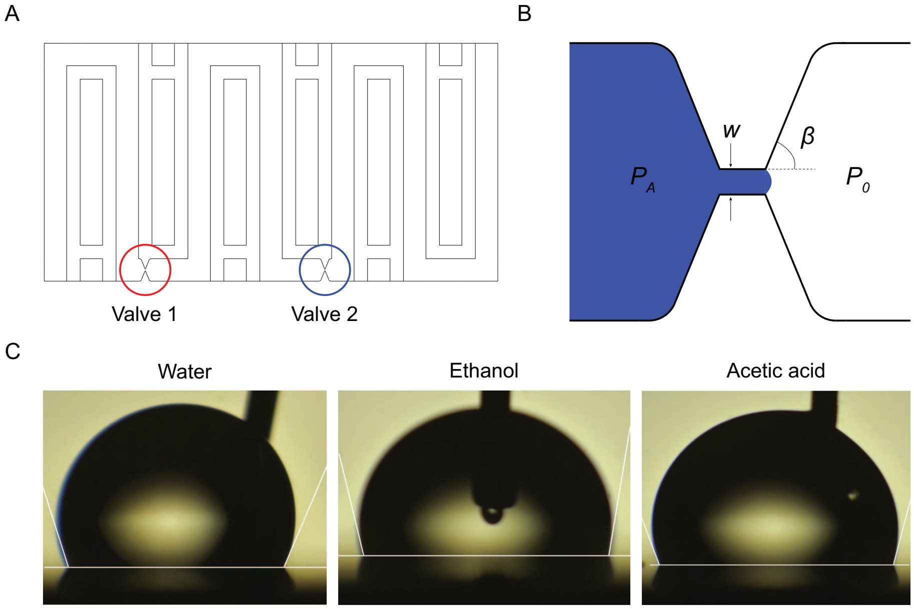

Figure 3.8: (A) Multi-mode morphing network design using capillary burst valves. (B) Schematics of a capillary burst valve. (C) Using sessile-drop goniometry, advancing contact angle of water, ethanol (11%), and acetic acid (10%) were measured.

withstand pressures for each valve can be determined using the following Young-Laplace equation

$$P_A - P_0 = -2\sigma(\frac{\cos\theta_I^*}{w} + \frac{\cos\theta_A}{h}), \tag{3.4}$$

where θ_I^* is the minimum between $\theta_A + \beta$ and 180°. θ_A is the critical advancing contact angle, and channel depth was fixed at $h = 1000\ \mu$m. Dimensions are shown in Fig. 3.8B. Using sessile-drop goniometry, we found the following data for the three liquids used in our experiments.

	Water	Ethanol (11%)	Acetic acid (10%)
Surface tension (mN/m)	72.0	46.0	37.9
θ_A (°)	118.3	99.6	108.0
$\theta_A + \beta$ (°)	186.0	167.3	175.7
$\cos\theta_I^*$	-1	-0.976	-0.997

Table 3.1: Information per liquid used in our experiments.

Advancing contact angle was found by capturing images as shown in Fig. 3.8C. Using the information in in table 3.1, we can find that $\cos\theta_I^*$ is approximately -1, and $w \gg h$ from our fixed channel depths and rough dimension of channel height of $w = 150\mu$m. We can thus simplify equation 3.4 to the equation below

$$P_A - P_0 = \frac{2\sigma}{w}. \tag{3.5}$$

Using equation 3.5, we can thus determine the dimensions of valve 1 and valve 2 that will show overlapping withstand pressures of each liquid. We design the valve channel height such that at a fixed pressure, water will reach but not pass through valve 1, ethanol (11%) will reach but not pass through valve 2, and finally acetic acid (10%) will pass through valve 2. The following information is shown in table 3.2.

Initially, when no liquid is inserted in the SPL, there will be no resistance to morphing as shown in Fig. 3.9A. For liquids, if we insert each of the three liquids with the same pressure (for example, 600 kPa), we obtain the

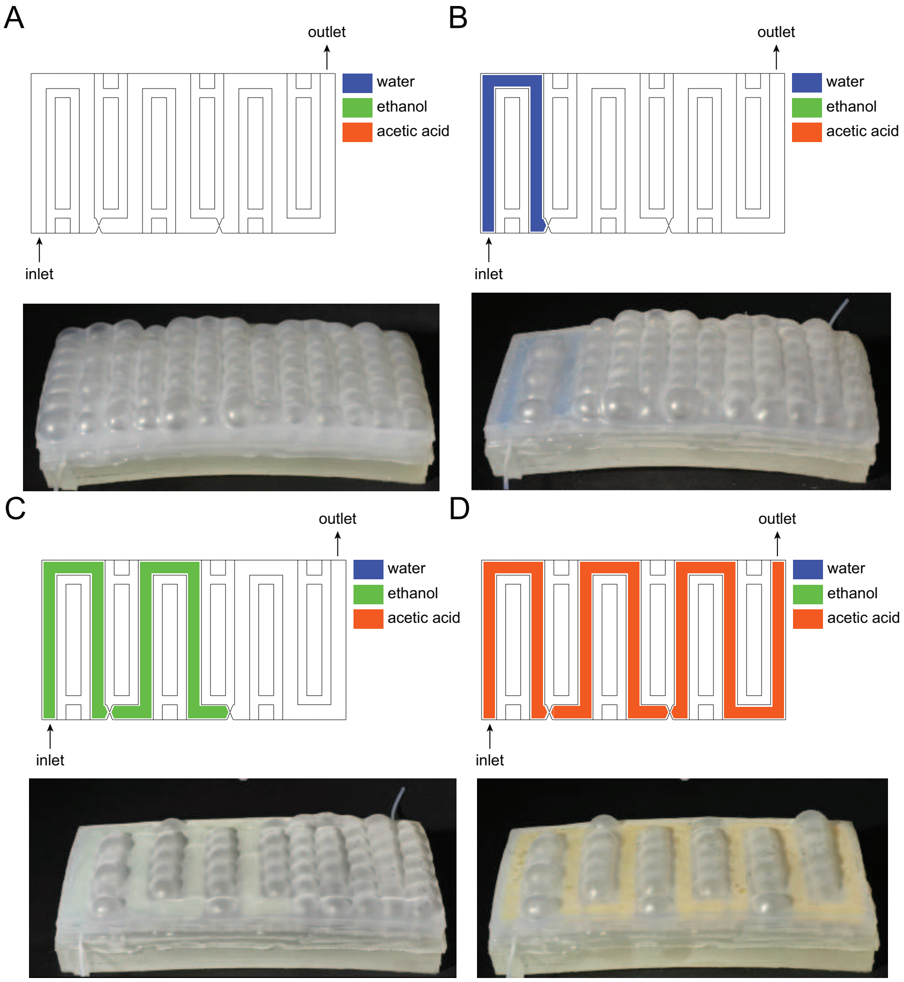

Figure 3.9: Schematics and morphing sequence of different liquids filled in the SPL. Initially when (A) air is filled, then (B) water, then (C) ethanol (11%), then (D) acetic acid (10%). Each experiment was conducted using the same pneu-net device by interchanging the liquid then freezing it.

	Max pressure (Pa)		
	Water	Ethanol (11%)	Acetic acid (10%)
Valve 1 (163μm)	883	590	465
Valve 2 (131μm)	1099	735	578

Table 3.2: Valve dimensions determined by withstand pressure of each liquid.

following. For water, because the max pressure, or withstand pressure for valves 1 and 2 are above 600 kPa, water will stop at valve 1. Upon freezing the liquid, the SPL would be patterned as shown in Fig. 3.9B. By pressurizing the actuation layer, the pneumatic device would inflate all areas apart from where the frozen water is. By melting the water and removing it using a syringe, we can then insert ethanol (11%) into the device using the same input pressure. Because 600 kPa is sufficient to pass through valve 1 for ethanol, it will form a different design as shown in Fig. 3.9C. Similarly, we can melt and remove the ethanol to test with acetic acid. Both valves cannot withstand 600 kPa for acetic acid, enabling the acetic acid to fully travel past both valves as shown in Fig. 3.9D. Thus, using a single pneu-net, we have shown how changing the liquid can lead to different channel designs, and ultimately different morphologies when actuated. Fully utilizing the property of surface tension of liquids by integrating a capillary burst valve enables for multi-mode morphing depending on the type of liquid without having to increase the number of input.

3.5 Multi-mode morphing of SPL embedded pneu-net

A multi-mode morphing cylindrical pneu-net device with embedded semicircular SPL chambers that have either a gas, liquid or solid filled in each chamber, as shown in Fig. 3.10, can be designed. The device has 20

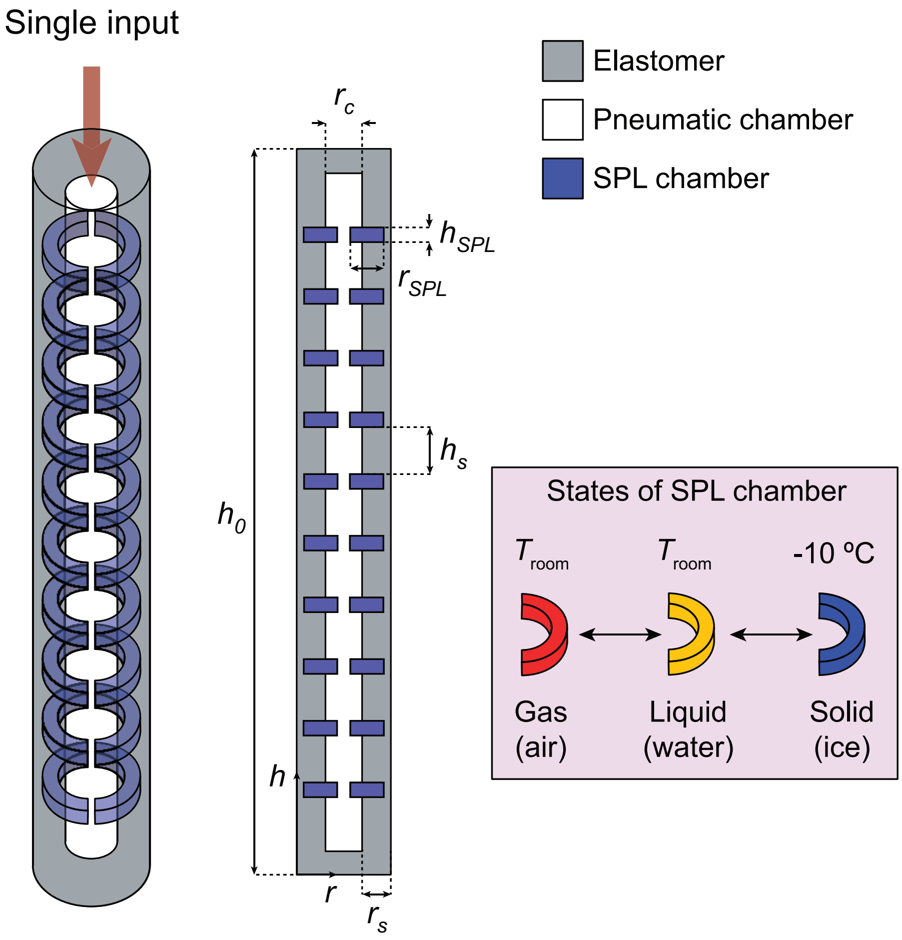

Figure 3.10: Schematics of a multi-mode morphing pneu-net with semicircular SPLs. Three states of matter exist inside each SPL chamber (gas, liquid, solid) which are shown in red, yellow, and blue, respectively.

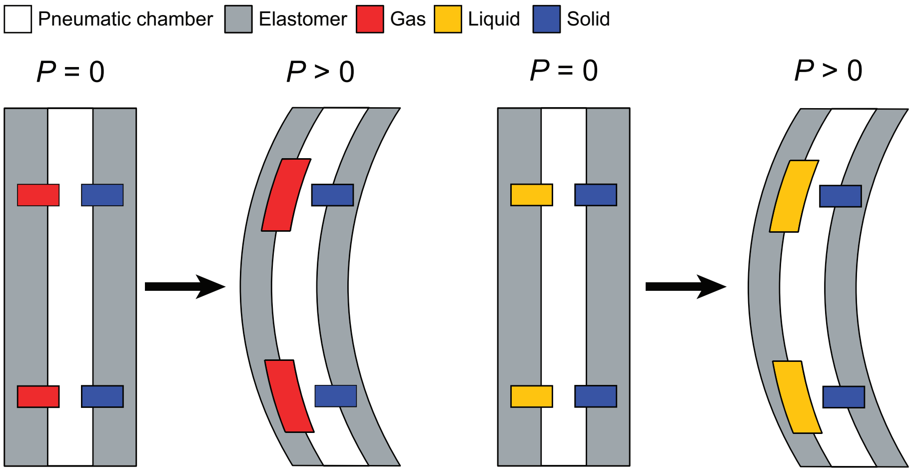

Figure 3.11: Design of SPL chamber to make the device bend. The device will bend towards where ice is filled.

evenly spaced SPL chambers surrounding a central pneumatic chamber for actuation made of Ecoflex 30. All individual SPL chambers are not connected with each other, and is filled using a syringe. Using plastic molds to manufacture the pneu-net device, its initial state has air filling each SPL chamber. After filling them with water using the syringe, the state can then be changed to solid by freezing the water inside a temperature controlled chamber at -10 °C. In the following, we use heat to melt specific SPL channels to 'pattern' a design, then actuate the pneumatic chamber to show different morphologies to achieve multi-mode morphing. Melting all SPL channels and simply refreezing it enables the device to be patterned again, making the system reprogrammable.

Figure 3.11 show how bending of the pneu-net device is achieved through anisotropic filling of SPL chambers. For instance, if SPL chambers on the left are filled with air, and the right filled with ice, the pneu-net device will bend towards the right upon inflation of the pneumatic chamber. Similarly, if SPL chambers on the left are filled with water, and the right filled with ice, the device will bend towards the left. This is achieved by using the difference in effective stiffness of fluid and solid, which we explained in §3.2 and showed through experiments in §3.3. Using different states of matter in each SPL chamber to modulate effective stiffness, we can design a single pneumatic device capable of different types of morphing using a single input.

First, when all SPL chambers are filled with air or water as shown in Fig. 3.12A and B, the device inflates isotropically in both h and r axes, upon inflation of the central pneumatic chamber. If all SPL chambers are filled with ice as shown in Fig. 3.11C, when inflated to the same pressure P_1, the device is uncapable of deforming due to the high effective stiffness of ice contained SPL chambers. From this state, if we melt the SPL chambers on the right through heating using a hot plate as shown in Fig. 3.11D, the device will bend towards the left (which we define as having positive curvature). Similarly, if all SPL chambers on the left are emptied and filled with air, while keeping SPL chambers on the right with ice as shown in Fig. 3.12E, the device will bend towards the right upon inflation forming a negative curvature. If only four SPL chambers located in the middle are filled with ice while all others are filled with air, the device will form a dumbbell shape upon inflation as shown in Fig. 3.12F.

Our pneu-net device can multi-mode morph using different configurations of states of matter inside the SPL chambers, without the need of sophisticated control inputs which are required in conventional soft robots that is difficult to control. We demonstrated how phase transition can be used to control local effective stiffness within a single pneu-net device capable of different types of morphing.

3.6 Pixelated multi-mode morphing

Here, we present a pixelated multi-mode morphing pneu-net to control each pixel using heat. In the previous section §3.5, we demonstrated how SPL chambers can be used to show multi-mode morphing and also be reprogrammable by melting and refreezing. The cylindrical pneu-net device

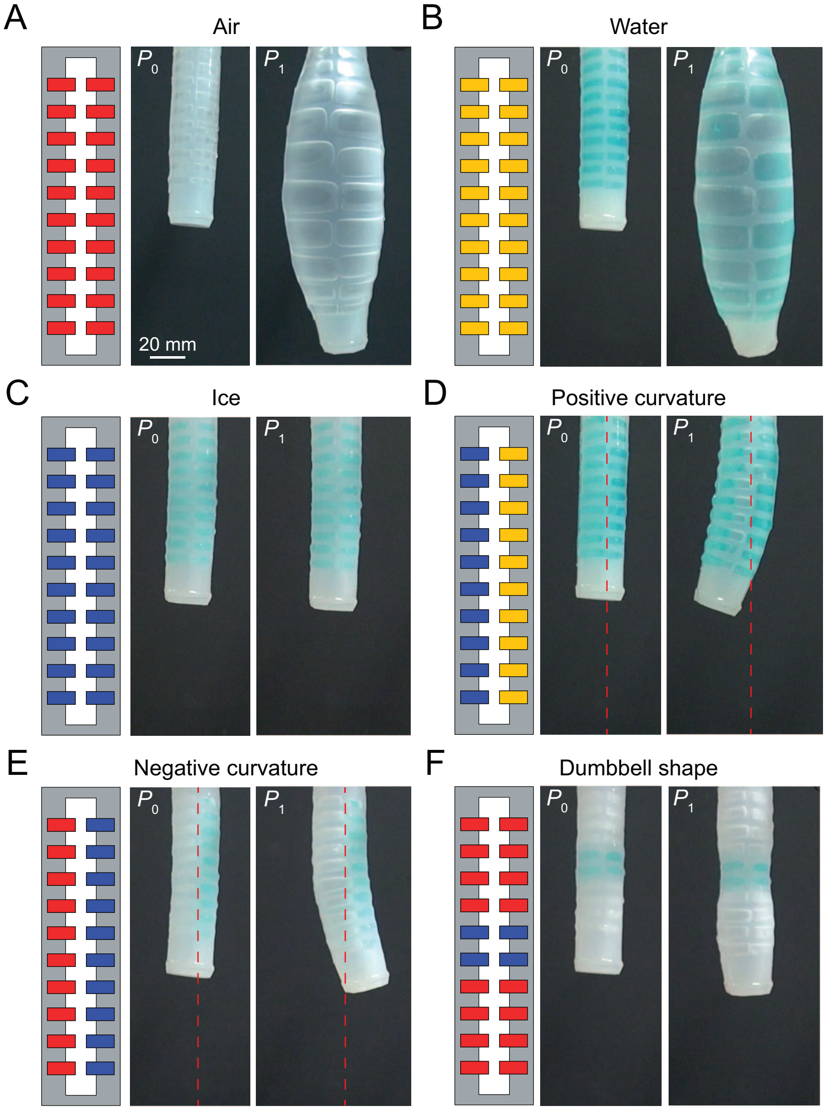

Figure 3.12: Experimental images of the device undergoing morphing from the undeformed initial configuration (left). As the actuation pressure increases (right), depending on the SPL chamber design in which different states exist in each chamber, the device can inflate radially and stretch (A, B), resist morphing (C), bend to the left (D), bend to the right (E) or morph into a dumbbell shape (F).

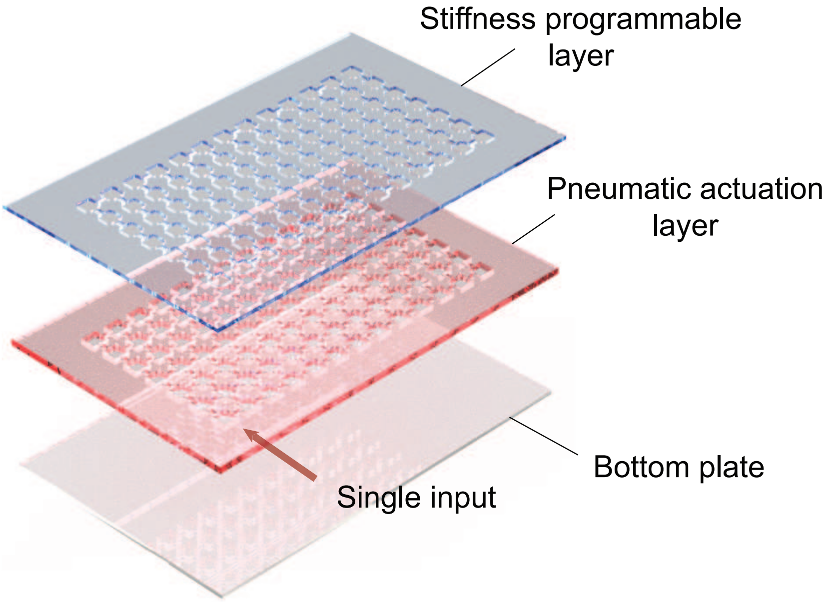

Figure 3.13: Schematics of how a pixelated multi-mode morphing pneu-net is made. Top layer is composed of stiffness-programmable layer, middle layer is composed of pneumatic actuation layer, and bottom layer is composed of the same elastomer, but thicker.

was focused in performing bending, stretching, and local stretching. Here, we focus on the ability to create any shape by interacting with the environment, acting as a morphing tangible display. The schematics of this device is shown in Fig. 3.13, which is composed of 3 layers. The top layer is designed to act as a stiffness programmable layer, with square pixels that are not connected to each other. The middle layer acts as a pneumatic actuation layer with all cells interconnected to be actuated using only a single input. The bottom layer is composed of the same material with greater thickness than the other two layers to ensure the inflation deforms the cells upwards, not downwards. pneu-net device is made of Ecoflex 45 Near Clear, which is a translucent, soft elastomer. Each layer is bonded to each other using a thin layer of uncured Ecoflex 45 Near Clear.

We filled each SPL chamber with air, water, and ice, then actuated the pneumatic layer to observe how the pneu-net device morphs. In its bonded state right after all three layers are combined, the pneu-net device contains air in all of its SPL chambers as shown in Fig. 3.14. When actuated, we can observe that all pixels inflate upwards by the same amount. In the case of water, using a syringe, we fill each pixel with blue color-dyed distilled water, then fill in the hole created by the syringe using Ecoflex 45 Near Clear and wait for it to cure. Upon actuation, we observe the same morphology as the one above as both gas and liquid do not contribute to the effective stiffness of each pixel. Then, we put the device in a temperature controlled chamber at -10 °C to freeze the water in the SPL pixels. Upon actuation, the ice greatly increases the effective stiffness of each pixel, preventing it to deform upwards.

Using our device, we can pattern different designs to activate wanted pixels by starting from an initial state of freezing all the pixels as shown in Fig. 3.17. There are various ways to melt the pixels. Rather than using an embedded heating device installed inside the pneumatic device, which would make it far more complicated, heavy, expensive, and harder to control, we choose to use external heat sources to melt specific pixels.

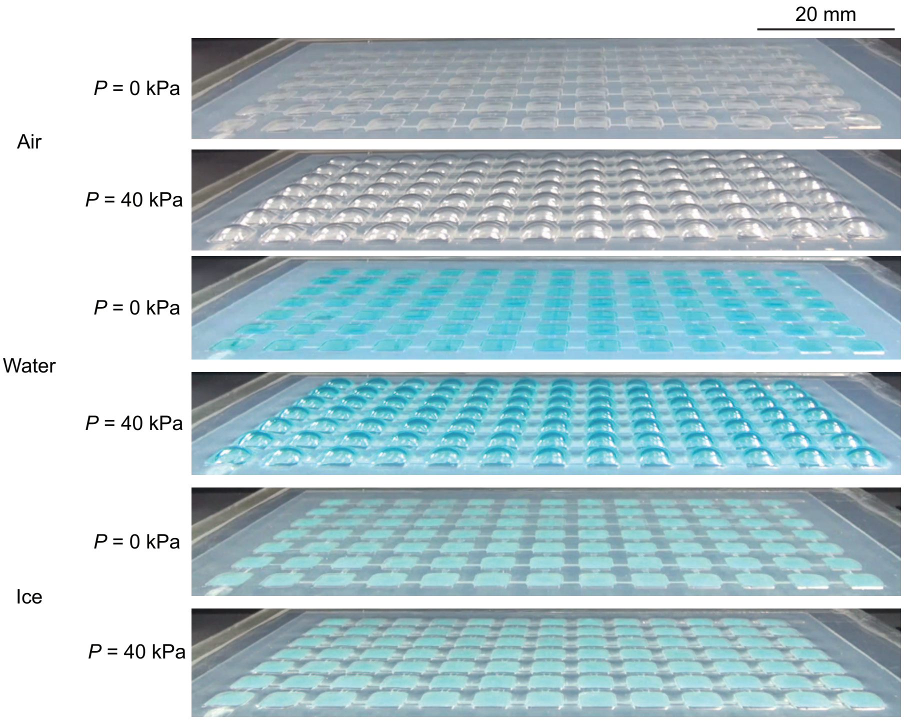

Figure 3.14: Experimental images of a pixelated multi-mode morphing pneu-net with air, water, and ice filled in the SPL. When pneumatic layer is actuated by pressurizing to 40 kPa, air and water show simultaneous morphing of all cells, whereas ice shows resistance to morphing.

We can either use a heat gun with a focused nozzle, or use our fingers to use body heat to melt the pixels.

For the first morphology 1 shown in Fig. 3.17 on the left, we melt the pixels shown in yellow inside a temperature controlled chamber at -10 °C. After melting the wanted pixels, we then actuate the device by pressurizing the pneumatic layer to 40 kPa. The letters 'SNU' that were melted can be seen to inflate upwards, while all other pixels resist deformation. Then, we can decrease the pressure back to 0 kPa, then melt the device at room temperature. After a few minutes, all the ice inside the SPL pixels melt to become water. Then, we freeze all the water inside the pixels to return to our initial state.

For our second morphology, we chose letters from a Braille display to show that pixelated pneu-net is not used only for display, but can also be used for its morphing capabilities, making it tangible. Not only can we met the pixels using our hand which makes it tangible, we can also feel with our hands which cells deformed up, and which didn't. This can be used for the visually disabled, as they are able to feel the pixels to read letters. The pixels shown in white boundaries on the right are melted using a heat gun, which is then pressurized to activate the pixels holding water. Then, the device can be melted then refrozen to return to its initial state, ready to be morphed to a different morphology.

Our device can also be used to show reversible plasticity. Previously, inside a temperature controlled chamber, we melt wanted pixels using a heating device and once all wanted cells are melted, we actuate the device at room temperature to morph into the wanted shape. However, if we actuate the device inside the temperature controlled chamber and keep it at constant pressure while melting the cells, we can observe individual cells morph as they are melted, then refreeze to sustain their form as the water quickly freezes after the heat is removed. This is shown in Fig. 3.15. First, the initial pixelated morphing sheet contains ice inside the temperature controlled chamber which is seen in Fig. 3.15A. Then, using a heating device, we melt wanted pixels inside the chamber as shown in Fig. 3.15B.

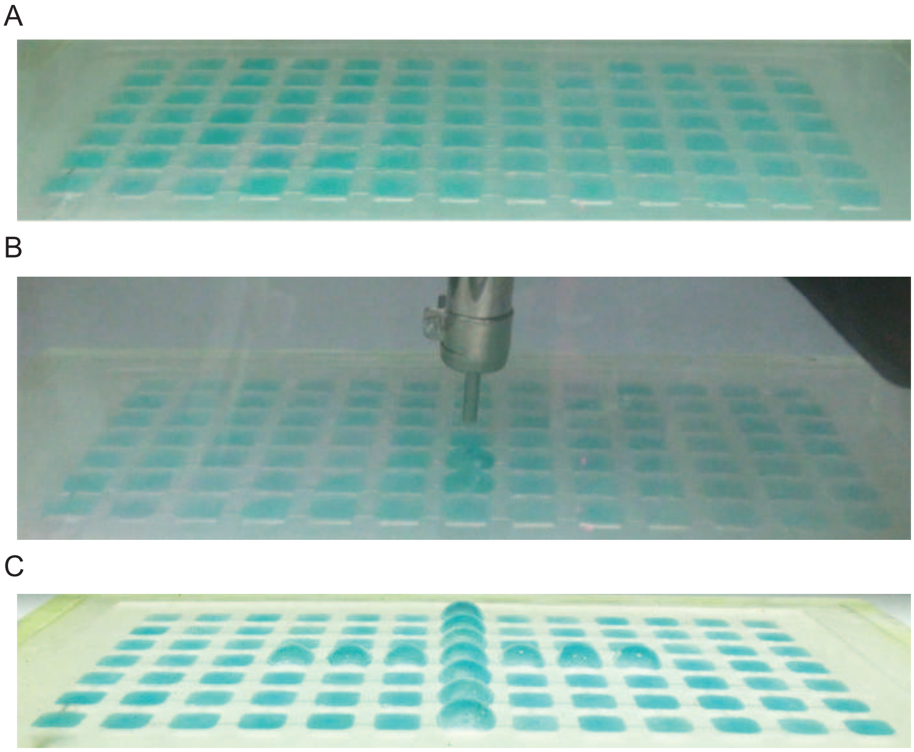

Figure 3.15: (A) Initial pixelated morphing sheet with all water inside SPLs frozen. (B) Melting specific cells (C) to create a '+' morphology.

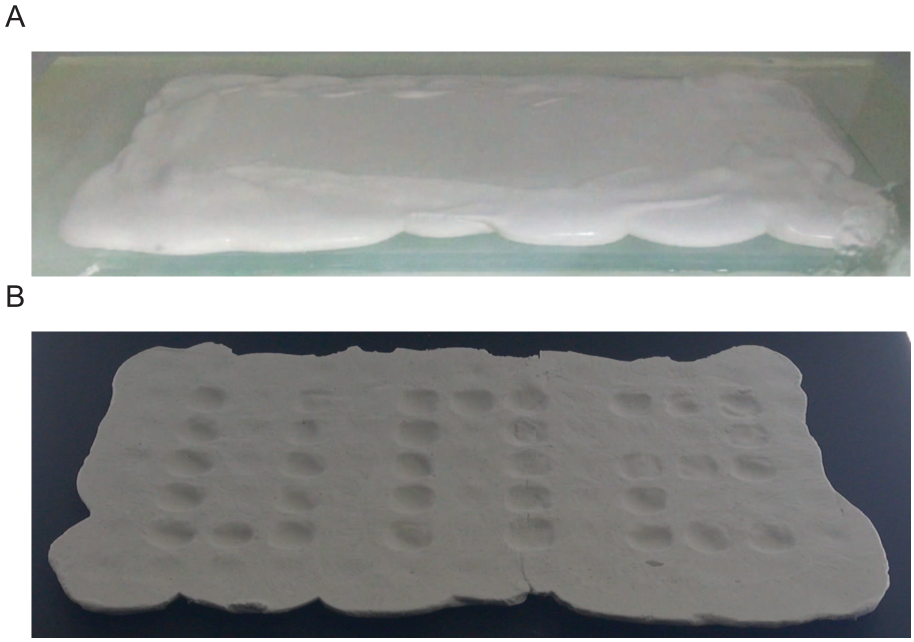

Figure 3.16: 'SNU' cells that are actuated can be (A) molded using gypsum to create an (B) 'SNU' mold.

Finally, after all the wanted pixels are melted, we can see a cross shape morphed while all other pixels remain flat. Even without supplying a constant pressure afterwards, the morphology will remain the cross shape, as the ice behaves plastic and maintains the shape. If we melt all the cells and refreeze them, it will return to its original state at Fig. 3.15A, ready to be morphed into a different shape.

Using our SPL embedded pneu-net to exhibit reversible plasticity characteristics, we can apply this trait to create a mold. Fig. 3.16A shows gypsum poured on top of the pneu-net device that has been plastically morphed without the need of air pressure, into the shape of SNU. We chose gypsum as it is able to solidify at subzero temperatures, as does not interact with elastomers which makes it easy to remove after molding. Then, we can remove the mold once the gypsum has solidified, resulting in an SNU mold as shown in Fig. 3.16B. Using this approach, we are able to use our pixelated pneu-net as a molding device to morph into different shapes depending on which cells we melt, then use gypsum or other molding material to create molds that are easy to make without having to use multiple molds which can be extremely costly and wasteful as conventional molding methods require the use of CNC machines to create accurate metal molds, or 1-time use through 3D printers.

We demonstrated how our pixelated pneu-net can be used to morph to two different morphologies, but our device is not limited to a fixed number of shapes, but can be limitless depending on which pixels we modulate stiffness. For example, shapes such as a heart, car, smiley face, or a boat can also be 'drawn' on our device to show how high the degree of freedom is by splitting a sheet into numerous pixels. The dimensions of our device was created to be used by human hands, roughly setting the size of a single pixel to that of a finger. The top wall thickness of our top and middle layers were set to 300 μm to ensure the deformation of pixels is clearly visible and sufficient to distinguish between activated and non-activated pixels.

Although we used water in our experiments, this device is not limited to using heat as an extra stimulus to control stiffness, but other stimuli such as magnetic, electric, chemical, or light can be used to modulate stiffness of each pixel. For example, if we fill the pixels with gallium, we do not have to use a temperature controlled chamber, but can phase transition solid to liquid using only our body temperature. However, the disadvantage of using such material would be the cost. Another example could be to use gold nanoparticles mixed with water that give off heat when exposed to a certain wavelength of light. Green laser can be used to heat individual cells to create the same effect as we have shown.

3.7 Conclusions

In this chapter, we have shown how to achieve multi-mode morphing pneu-nets using an embedded stiffness programmable layer into the top wall of a standard pneu-net. Conventional pneu-nets have a predetermined

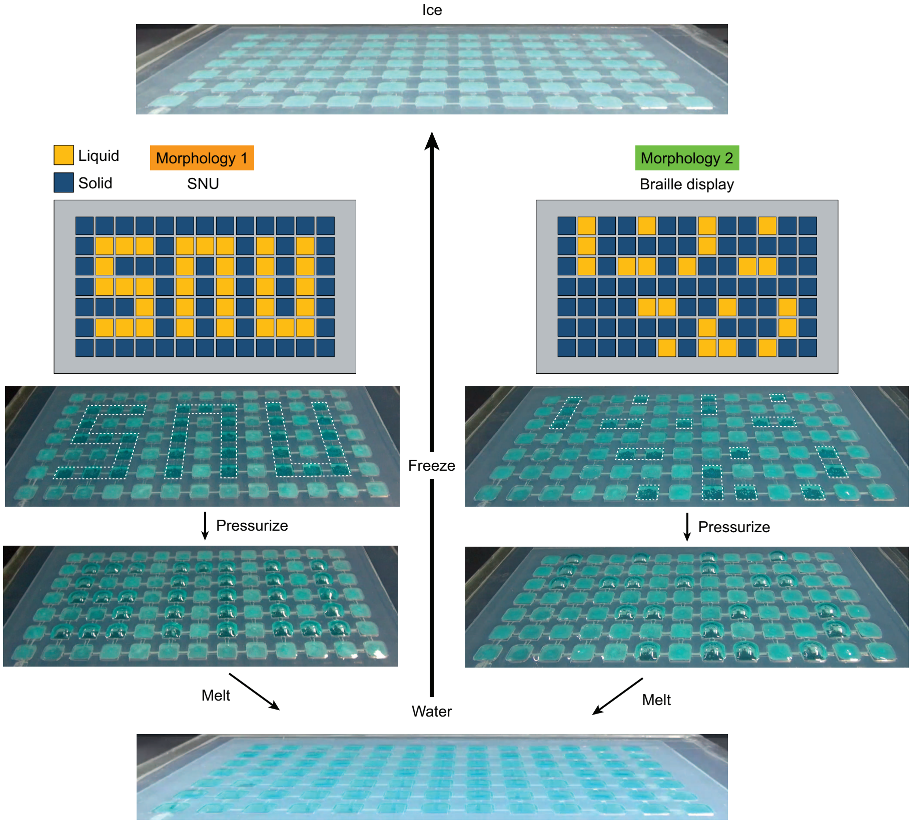

Figure 3.17: Reprogrammable pixelated pneu-net showing two different designs. On the left, 'SNU' cells are melted using a heat gun, then pressurized to show the melted cells morphing while all others don't. On the right, using Braille display, an example of letters that can be read by visually disabled people by touching the surface has been shown. Both designs can then be melted, then refrozen to return to its initial state.

designated shape upon actuation, which limits the use as different morphologies require new pneu-nets to be made. However, by adding a simple stiffness control layer, we can use a single pneu-net to morph multiple times which would increase the functionality and morphology, eliminating the constraints of a pneu-net while keeping the advantage of rapid actuation. Using a simple trilayer model, we showed how the characteristics of a fluid and solid can be used to change the effective stiffness in the SPL. Using our results, we experimentally showed the resistance to morph for solids, and ease of morph for fluids. Using liquid properties, strictly surface tension, we showed different channel designs depending on the liquid used by using a capillary burst valve. Applying our findings, we demonstrated two different multi-mode morphing pneumatic devices to show different types of multi-mode morphing. The first cylindrical pneu-net showed how different types of bending, stretching, and a dumbbell shape can be created from a single pneu-net. Our pixelated pneu-net showed how a flat pneumatic sheet can interact with the environment to create different shapes and letters without having to create a complicated system by embedding circuits into the pneu-net (Hwang *et al.*, 2022). We believe that we have introduced a simple yet effective method with promising possibilities to improve the current state-of-the-art soft robots to perform complicated tasks without having to increase the control complexity of the system.

Chapter 4

Concluding remarks

Our focus of our research was on creating a more efficient soft robotic system without having to increase the control complexity, or requiring a complicated manufacturing procedure. We aimed to use a simple yet extremely effective method to create multi-morphing soft actuators, that can be implemented into existing systems. Using the advantages of pneumatic actuators of being cheap, easy to manufacture, and rapid actuation speed, we increase the degree of freedom of morphing without compromise to show the potential of future soft robots. In this chapter, we first summarize our research findings in §4.1, then propose future works based on our research in §4.2.

4.1 Summary of findings

Using the basic principle of pneu-nets, we developed a multi-morphing pneu-net device using two different methods. First, we use the inherent property of strain-hardening that exists for elastomers which makes it possible for the material to change stiffness depending on strain. This does not require any special manufacturing methods and can be implemented into any existing pneu-nets to morph more than once. Second, we introduced an different method to modulate stiffness through a stiffness programmable layer using an abundant material, water. Through phase transition, we showed that stiffness can be controlled and explained theoretically using a trilayer beam, the difference between the property of fluids and solids. For both methods, we showed applications to perform various tasks without having to increase the control complexity of the system.

In chapter 1, we introduced the state-of-the-art research for soft actuators and how they differentiate themselves from hard robots. Various stimuli responsive soft actuators show high degree of freedom, but require complex manufacturing methods or are hard to control. We stress the importance of developing a multi-morphing soft robot that can perform various tasks without being too expensive, require numerous inputs which makes it hard to control, or have a lengthy manufacturing method.

In chapter 2, we harnessed the strain-hardening effect of soft elastomers to create a multi-morphing pneu-net. We first showed how strain-hardening elastomers have regions of softening and hardening which enables modules within a single pneu-net to activate at different distinct pressures. We change material and geometry of a pneumatic network to achieve various multi-morphing: bending–twisting, stretching–bending, and bending–bending. Using our theoretical model, we solved using Gent theory how a unit cell would deform when subject to pressure while exhibiting strain-hardening as it is stretched. Then, using numerical simulations, we were able to design multiple sequential morphing pneu-nets to perform various tasks. For example, our bending–twisting pneu-net was able to grasp, then twist an object to turn on a bulb or open a door. Our stretching–bending pneu-net was able to seal and move a flask from an unwanted environment, or could be used to design a self-standing crawler. Bending–bending pneu-net was used to grasp two different objects at different sides using positive and negative curvatures of each region. We showed that conventional pneu-nets can have increased morphing modes if the strain-hardening effect is used accordingly. The manufacturing method required is identical of that of a normal pneu-net, thus having no drawbacks to using this approach.

In chapter 3, we proposed another method to achieve multi-morphing of pneu-nets through the use of phase transition. Using a simple trilayer beam to model the top wall of a pneu-net, we showed that depending on what material exists in the middle layer sandwiched between two elastomer walls, the effective stiffness of the structure can be calculated. In the case of fluids, they cannot contribute to stiffness thus having low effective stiffness. We showed that for the case of ice, it greatly increases the effective stiffness, thus enabling us to control stiffness using liquid–solid phase transition. Using our findings, we experimentally demonstrated that for a unit cell, fluids encapsulated inside a stiffness programmable layer (SPL) can easily deform, whereas a solid like ice can resist deforming for the same pressure range. We then showed using surface tension of different liquids, we can integrate a capillary burst valve to control how far a liquid can travel using a constant input pressure. Then, we showed two multi-morphing designs, one in the shape of a cylinder to show various morphologies such as bending, stretching, and even a shape of a dumbbell. Finally, we showed a pixelated multi-morphing device capable of interacting with the environment to create various shapes and letters that can be used for visual and tangible purposes such as a Braille display.

4.2 Future works

We increased the morphing mode of conventional pneu-nets using two different approaches: strain-hardening effect of elastomers, and phase transition of liquid–solid. We showed several design methods and applications, but we believe there are a lot of potential future works related to our research which could further the progress of multi-morphing pneumatic systems.

Multi-morphing of pneumatic networks through strain-hardening

Our research focused on creating a sequential morphing device that can perform two types of deformations rather than one from a single input. However, our findings are not only limited to dual-morphing, but can be designed to perform tri-morphing or quad-morphing. Theoretically, by controlling the material used to strain-harden at different distinct pressures as well as designing the geometry of each section differently, a bending–stretching–twisting robot can be made, for example. We also used conventional materials used in pneu-nets made by Smooth-On products, but strain-hardening is also observed in other soft materials such as hydrogels. This can increase the stimuli used to control the soft robot without requiring extra manufacturing processes as it can interact with the environment to morph. By installing bistable structures within the pneu-net, we can also make it easier to distinguish between each morphing, making it more suitable to be used in real life applications. In order to develop these goals, numerical simulations using different materials must be conducted to then be made experimentally and tested.

Multi-morphing of pneumatic actuators through phase transition

In this chapter, we introduced using a simple concept of phase transition of liquid–solid to change the local stiffness within a pneumatic system. The liquid we used was mainly water, and we used ethanol and acetic acid to show the potential of using different liquids by exploiting properties only liquids have. However, we believe that this is not limited to just using water, but could work for any liquid–solid phase transition material depending on the use of the system. For example, using magnetic-responsive liquids could be used to respond with magnetic fields, or a photo-responsive particle could be mixed with a liquid to respond to a specific wavelength of light. Furthermore, we introduced a cylindrical pneu-net for various multi-morphing shapes, and a pixelated device to interact with the environment, but the shape does not need to be limited to just cylindrical or a plate. A more complex device can be manufactured to suit the needs of a task, that is still easily controlled using a single input. By using different liquids or changing the elastomer used, the degree of morphing can be increased greatly to perform increased number of functions without having to use complicated control mechanisms. We believe that in the future, these approaches can create huge impacts on soft robotics, and to our daily lives.

References

Adler, P.H., Olson, G.B. & Owen, W.S. (1986). Strain hardening of hadfield manganese steel. *Metallurgical and Materials Transactions A*, **17**, 1725–1737.

Aghakhani, A., Yasa, O., Wrede, P. & Sitti, M. (2020). Acoustically powered surface-slipping mobile microrobots. *Proceedings of the National Academy of Sciences*, **117**, 3469–3477.

Aksoy, B. & Shea, H. (2020). Reconfigurable and latchable shape-morphing dielectric elastomers based on local stiffness modulation. *Advanced Functional Materials*, **30**, 2001597.

Alapan, Y., Karacakol, A.C., Guzelhan, S.N., Isik, I. & Sitti, M. (2020). Reprogrammable shape morphing of magnetic soft machines. *Science Advances*, **6**, eabc6414.

Allen, J.J., M Äthger, L.M., Barbosa, A., Buresch, K.C., Sogin, E., Schwartz, J., Chubb, C. & Hanlon, R.T. (2010). Cuttlefish dynamic camouflage: responses to substrate choice and integration of multiple visual cues. *Proceedings of the Royal Society B*, **277**, 1031–1039.

Allen, J.J., Bell, G.R.R., Kurizian, A.M., Velankar, S.S. & Hanlon, R.T. (2014). Comparative morphology of changeable skin papillae in octopus and cuttlefish. *Journal of morphology*, **275**, 371–390.

Amjadi, M. & Sitti, M. (2016). High-performance multiresponsive paper actuators. *ACS Nano*, **10**, 10202–10210.

Beatty, M.F. & Krishnaswamy, S. (2000). A theory of stress-softening in incompressible isotropic materials. *Journal of the Mechanics and Physics of Solids*, **48**, 1931–1965.

Belding, L., Baytekin, B., Baytekin, H.T., Rothemund, P., Verma, M.S., Nemiroski, A., Sameoto, D., Grzybowski, B.A. & Whitesides, G.M. (2018). Slit tubes for semisoft pneumatic actuators. *Advanced Materials*, **30**, 1704446.

Buckingham, E. (1914). On physically similar systems; illustrations of the use of dimensional analysis. *Physical Review*, **4**, 345.

Butkovich, T.R. (1959). Mechanical properties of ice. *Proceedings of the 3rd U.S. Symposium on Rock Mechanics*, 351–360.

Cantournet, S., Desmorat, R. & Besson, J. (2009). Mullins effect and cyclic stress softening of filled elastomers by internal sliding and friction thermodynamics model. *International Journal of Solids and Structures*, **46**, 2255–2264.

Cho, H., Kim, H.Y., Kang, J.Y. & Kim, T.S. (2007). How the capillary burst microvalve works. *Journal of Colloid and Interface Science*, **306**, 379–385.

Cui, Y., Tan, M., Zhu, A. & Guo, M. (2014). Strain hardening and highly resilient hydrogels crosslinked by chain-extended reactive pseudo-polyrotaxane. *Royal Society of Chemistry Advances*, **4**, 56791–56797.

Deng, Z., Hu, T., Lei, Q., He, J., Ma, P.X. & Guo, B. (2019). Stimuli-responsive conductive nanocomposite hydrogels with high stretchability, self-healing, adhesiveness, and 3d printability for human motion sensing. *ACS Applied Materials and Interfaces*, **11**, 6796–6808.

Dong, Y., Wang, J., Guo, X., Yang, S., Ozen, M.O., Chen, P., Liu, X., Du, W., Xiao, F., Demirci, U. & Liu, B.F. (2019). Multi-stimuli-responsive programmable biomimetic actuator. *Nature Communications*, **10**, 4087.

Dong, Y., Wang, L., Xia, N., Yang, Z., Zhang, C., Pan, C., Jin, D., Zhang, J., Majidi, C. & Zhang, L. (2022). Untethered small-scale magnetic soft robot with programmable magnetization and integrated multi-functional modules. *Science Advances*, **8**, eabn8932.

Elbaum, R., Zaltzman, L., Burgert, I. & Fratzl, P. (2007). The role of wheat awns in the seed dispersal unit. *Science*, **316**, 884–886.

Esser, F.J., Auth, P. & Speck, T. (2020). Artificial venus flytraps: A research review and outlook on their importance for novel bioinspired materials systems. *Frontiers in Robotics and AI*, **7**, 75.

Evangelista, D., Hotton, S. & Dumais, J. (2011). The mechanics of explosive dispersal and self-burial in the seeds of the filaree, erodium cicutarium (geraniaceae). *Journal of Experimental Biology*, **214**, 521–529.

Forterre, Y., Skotheim, J.M., Dumais, J. & Mahadevan, L. (2005). How the venus flytrap snaps. *Nature*, **433**, 421–425.

Galant, O., Bae, S., Silberstein, M.N. & Diesendruck, C.E. (2019). Highly stretchable polymers: mechanical properties improvement by balancing intra- and intermolecular interactions. *Advanced Functional Materials*, **30**, 1901806.

Gent, A.N. (1996). A new constitutive relation for rubber. *Rubber Chemistry and Technology*, **69**, 59–61.

Gerbode, S.J., Puzey, J.R. & McCormick, A.G. (2012). How the cucumber tendril coils and overwinds. *Science*, **337**, 1087–1091.

Gu, G.Y., Zhu, J., Zhu, L.M. & Zhu, X. (2017). A survey on dielectric elastomer actuators for soft robots. *Bioinspiration and Biomimetics*, **12**, 011003.

Gutierrez-Urrutia, I. & Raabe, D. (2012). Grain size effect on strain hardening in twinning-induced plasticity steels. *Scripta Materialia*, **66**, 992–996.

Han, B., Ma, Z.C., Zhang, Y.L., Zhu, L., Fan, H., Bai, B., Chen, Q.D., Yang, G.Z. & Sun, H.B. (2022). Reprogrammable soft robot actuation by synergistic magnetic and light fields. *Advanced Functional Materials*, **32**, 2110997.

Hao, X.P., Zhang, C.W., Zhang, X.N., Hou, L.X., Hu, J., Dickey, M.D., Zheng, Q. & Wu, Z.L. (2022). Healable, recyclable, and multifunctional soft electronics based on biopolymer hydrogel and patterned liquid metal. *Small*, **18**, 2201643.

Haward, R.N. (1993). Strain hardening of thermoplastics. *Macromolecules*, **26**, 5860–5869.

Hawkes, E.W., Blumenschein, L.H., Greer, J.D. & Okamura, A.M. (2017). A soft robot that nagivates its environment through growth. *Science Robotics*, **2**, eaan3028.

Hu, S., Cao, X., Reddyhoff, T., Ding, X., Shi, X., Dini, D., deMello, A.J., Peng, Z. & Wang, Z. (2022). Pneumatic programmable superrepellent surfaces. *Droplet*, **1**, 48–55.

Hu, W., Lum, G.Z., Mastrangeli, M. & Sitti, M. (2018). Small-scale soft-bodied robot with multimodal locomotion. *Nature*, **554**, 81–85.

Huang, G., Zhang, H., Liu, Y., Chang, H., Zhang, H., Song, H., Xu, D. & Shi, T. (2017). Strain hardening behavior of poly(vinyl alcohol)/borate hydrogels. *Macromolecules*, **50**, 2124–2135.

Hwang, D., Barron III, E.J., Tahidul Haque, A.B.M. & Bartlett, M.D. (2022). Shape morphing mechanical metamaterials through reversible plasticity. *Science Robotics*, **7**, eabg2171.

Kanjanapas, S., Munez, C.M., Williams, S.R., Okamura, A.M. & Luo, M. (2019). Design and analysis of pneumatic 2-dof soft haptic devices for shear display. *IEEE Robotics and Automation Letters*, **4**, 1365–1371.

Kashyap, V., Caprio, A., Doshi, T., Jang, S.J., Liu, C.F., Mosadegh, B. & Dunham, S. (2020). Multilayer fabrication of durable catheter-deployable soft robotic sensor arrays for efficient left atrial mapping. *Science Advances*, **6**, eabc6800.

Kaynak, M., Dirix, P. & Sakar, M.S. (2020). Addressable acoustic actuation of 3d printed soft robotic microsystems. *Advanced Science*, **7**, 2001120.

Kim, S.U., Lee, Y.J., Liu, J., Kim, D.S., Wang, H. & Yang, S. (2022). Broadband and pixelated camouflage in inflating chiral nematic liquid crystalline elastomers. *Nature Materials*, **21**, 41–46.

Kim, W., Byun, J., Kim, J.K., Choi, W.Y., Jakobsen, K., Jakobsen, J., Lee, D.Y. & Cho, K.J. (2019). Bioinspired dual-morphing stretchable origami. *Science Robotics*, **4**, eaay3493.

Kim, Y., Yuk, H., Zhao, R., Chester, S.A. & Zhao, X. (2018). Printing ferromagnetic domains for untethered fast-transforming soft materials. *Nature*, **558**, 274–279.

Kleemola, H.J. & Nieminen, M.A. (1974). On the strain-hardening parameters of metals. *Metallurgical transactions*, **5**, 1863–1866.

Lavazza, J., Contino, M. & Marano, C. (2023). Strain rate, temperature and deformation state effect on ecoflex 00-50 silicone mechanical behaviour. *Mechanics of Materials*, **178**, 104560.

Lee, B.P. & Konst, S. (2014). Novel hydrogel actuator inspired by reversible mussel adhesive protein chemistry. *Advanced Materials*, **26**, 3415–3419.

Lee, H., Kim, H., Ha, I., Jung, J., Won, P., Cho, H., Yeo, J., Hong, S., Han, S., Kwon, J., Cho, K.J. & Ko, S.H. (2019). Directional shape morphing transparent walking soft robot. *Soft Robotics*, **6**, 760–767.

Li, C., Yang, H., Suo, Z. & Tang, J. (2020). Fatigue-resistant elastomers. *Journal of the Mechanics and Physics of Solids*, **134**, 103751.

Li, S. & Wang, K.W. (2015). Fluidic origami: a plant-inspired adaptive structure with shape morphing and stiffness tuning. *Smart Materials and Structures*, **24**, 105031.

Li, X., Liu, J., Li, D., Huang, S., Huang, K. & Zhang, X. (2021a). Bioinspired multi-stimuli responsive actuators with synergistic color- and morphing-change abilities. *Advanced Science*, **8**, 2101295.

Li, Y., Li, W., Sun, A., Jing, M., Liu, X., Wei, L., Wu, K. & Fu, Q. (2021b). A self-reinforcing and self-healing elastomer with high strength, unprecedented toughness and room-temperature reparability. *Materials Horizons*, **8**, 267–275.

Liao, Z., Hossain, M., Yao, X., Navaratne, R. & Chagnon, G. (2020). A comprehensive thermo-viscoelastic experimental investigation of ecoflex polymer. *Polymer Testing*, **86**, 106478.

Marchese, A.D., Onal, C.D. & Rus, D. (2014). Autonomous soft robotic fish capable of escape maneuvers using fluidic elastomer actuators. *Soft Robotics*, **1**, 75–87.

Martinez, R.V., Branch, J.L., Fish, C.R., Jin, L., Shepherd, R.F., Nunes, R.M.D., Suo, Z. & Whitesides, G.M. (2012). Robotic tentacles with three-dimensional mobility based on flexible elastomers. *Advanced Materials*, **25**, 205–212.

Melancon, D., Gorissen, B., García-Mora, C.J., Hoberman, C. & Bertoldi, K. (2021). Multistable inflatable origami structures at the metre scale. *Nature*, **592**, 545–550.

Morin, S.A., Shepherd, R.F., Kwok, S.W., Stokes, A.A., Nemiroski, A. & Whitesides, G.M. (2012). Camouflage and display for soft machines. *Science*, **337**, 828–832.

Mu, J., Jung de Andrade, M., Fang, S., Wang, X., Gao, E., Li, N., Kim, S.H., Wang, H., Hou, C., Zhang, Q., Zhu, M., Qian, D., Lu, H., Kongahage, D., Talebian, S., Foroughi, J., Spinks, H., G. Kim, Ware, T.H., Sim, H.J., Lee, D.Y., Jang, Y., Kim, S.J. & Baughman, R.H. (2019). Sheath-run artificial muscles. *Science*, **365**, 150–155.

Must, I., Sinibaldi, E. & Mazzolai, B. (2019). A variable-stiffness tendril-like soft robot based on reversible osmotic actuation. *Nature Communications*, **10**, 344.

Naclerio, N.D., Karsai, A., Murray-Cooper, M., Ozkan-Aydin, Y., E., A., Goldman, D.I. & Hawkes, E.W. (2017). Controlling subterranean forces enables a fast, steerable, burrowing soft robot. *Science Robotics*, **6**, eaan3028.

Olivera, B.M., Gray, W.R., Zeikus, R., Mcintosh, J.M., Varge, J., Rivier, J., Santos, V.D. & Cruz, L.J. (1985). Peptide neurotoxins from fish-hunting cone snails. *Science*, **230**, 1338–1343.

Olivera, B.M., Seger, J., Horvath, M.P. & Fedosov, A.E. (2015). Prey-capture strategies of fish-hunting cone snails: behavior, neurobiology and evolution. *Brain, Behavior and Evolution*, **86**, 58–74.

Panetta, D., Buresch, K. & Hanlon, R.T. (2017). Dynamic masquerade with morphing three-dimensional skin in cuttlefish. *Biology letters*, **13**, 20170070.

Park, T., Kim, K., Oh, S.R. & Cha, Y. (2020). Electrohydraulic actuator for a soft gripper. *Soft Robotics*, **7**, 68–75.

Payne, C.J., Wamala, I., Bautista-Salinas, D., Saeed, M., Story, D.V., Thalhofer, T., Horvath, M.A., Abah, C., Del Nido, P.J., Walsh, C.J. & Vasilyev, N.V. (2017). Soft robotic ventricular assist device with septal bracing for therapy of heart failure. *Science Robotics*, **2**, eaan6736.

Pelrine, R., Kornbluh, R., Pei, Q. & Joseph, J. (2000). High-speed electrically actuated elastomers with strain greater than 100%. *Science*, **287**, 836–839.

Piskarev, Y., Shintake, J., Chautems, C., Lussi, J., Boehler, Q., Nelson, B.J. & Floreano, D. (2022). A variable stiffness magnetic catheter made of a conductive phase-change polymer for minimally invasive surgery. *Advanced Functional Materials*, **32**, 2107662.

Rumens, C.V., Ziai, M.A., Belsey, K.E., Batchelor, J.C. & Holder, S.J. (2015). Swelling of pdms networks in solvent vapours; applications for passive rfid wireless sensors. *Journal of Materials Chemistry C*, **3**, 10091–10098.

Sachin, Wang, Z. & Hirai, S. (2022). Analytical modeling of a soft pneu-net actuator subjected to planar tip contact. *IEEE Transactions on Robotics*, **38**, 2720–2733.

Shah, D.S., Powers, J.P., Tilton, L.G., Kriegman, S., Bongard, J. & Kramer-Bottiglio, R. (2021). A soft robot that adapts to environments through shape change. *Nature Machine Intelligence*, **3**, 51–59.

Shepherd, R.F., Ilievski, F., Choi, W., Morin, A., Stokes, A.A., Mazzeo, A.D., Chen, X., Wang, M. & Whitesides, G.M. (2011). Multigait soft robot. *Proceedings of the National Academy of Sciences*, **108**, 20400–20403.

Shin, B., Ha, J., Lee, M., Park, K., Park, G.H., Choi, T.H., Cho, K.J. & Kim, H.Y. (2018). Hygrobot: A self-locomotive ratcheted actuator powered by environmental humidity. *Science Robotics*, **3**, eaar2629.

Siéfert, E., Reyssat, E., Bico, J. & Roman, B. (2019). Bio-inspired pneumatic shape-morphing elastomers. *Nature Materials*, **18**, 24–28.

Singh, K., Gupta, S., Khosla, A. & Furukawa, H. (2023). Transforming soft robotics: laminar jammers unlocking adaptive stiffness potential in pneunet actuators. *ECS Journal of Solid State Science and Technology*, **12**, 047007.

Su, B., Gong, S., Ma, Z., Yap, L.W. & Cheng, W. (2015). Mimosa-inspired design of a flexible pressure sensor with touch sensitivity. *Small*, **11**, 1886–1891.

Swamynathan, S., Jobst, S., Kienle, D. & Keip, M.A. (2022). Phase-field modeling of fracture in strain-hardening elastomers: variational formulation, multiaxial experiments and validation. *Engineering Fracture Mechanics*, **265**, 108303.

Tawk, C., Gillett, A., in het Panhuis, M., Spinks, G.M. & Alici, G. (2019). A 3d-printed omni-purpose soft gripper. *IEEE Transcations on Robotics*, **35**, 1268–1275.

Thai, M.T., Hoang, T.T., Phan, P.T., Lovell, N.H. & Do, T.N. (2020). Soft microtubule muscle-driven 3-axis skin-stretch haptic devices. *IEEE Access*, **8**, 157878–157891.

Treloar, L.R.G. (1944). Stress-strain data for vulcanized rubber under various types of deformation. *Rubber Chemistry and Technology*, **17**, 813–825.

Vasios, N., Gross, A.J., S., S., Overvelde, J.T.B. & Bertoldi, K. (2020). Harnessing viscous flow to simplify the actuation of fluidic soft robots. *Soft Robotics*, **7**, 1–9.

Wang, F., Chen, B., Wu, L., Zhao, Q. & Zhang, L. (2020). In situ swelling-gated chemical sensing actuator. *Cell Reports Physical Science*, **1**, 100011.

Wang, H., Chen, S., Li, H., Chen, X., Cheng, J., Shao, Y., Zhang, C., Zhang, J., Fan, L., Chang, H., Guo, R., Wang, X., Li, N., Hu, L., Wei, Y. & Liu, J. (2021a). A liquid gripper based on phase transitional metallic ferrofluid. *Advanced Functional Materials*, **31**, 2100274.

Wang, Y., Li, L., Hofmann, D., Andrade, J.E. & Daraio, C. (2021b). Structured fabrics with tunable mechanical properties. *Nature*, **596**, 238–243.

White, F.M. (1991). *Viscous fluid flow*. McGraw-Hill, New York.

Yu, C.J., Duan, Z., Yuan, P.X., Li, Y., Su, Y., Zhang, X., Pan, Y., Dai, L.L., Nuzzo, R.G., Huang, Y., Jiang, H. & Rogers, J.A. (2013). Electronically programmable, reversible shape change in two-and three-dimensional hydrogel structures. *Advanced Materials*, **25**, 1541–1546.

Yuan, J., Neri, W., Zakri, C., Merzeau, P., Kratz, K., Lendlein, A. & Poulin, P. (2019). Shape memory nanocomposite fibers for untethered high-energy microengines. *Science*, **365**, 155–158.

Zhang, L.D., Desta, I. & Naumov, P. (2016). Synergistic action of thermoresponsive and hygroresponsive elements elicits rapid and directional response of a bilayer actuator. *Chemical Communications*, **52**, 5920–5923.

Zhang, S., Ke, X., Jiang, Q., Ding, H. & Wu, Z. (2021). Programmable and reprocessable multifunctional elastomeric sheets for soft origami robots. *Science Robotics*, **6**, eabd6107.

Zhang, X. & Oseyemi, A.E. (2022). A herringbone soft pneu-net actuator for enhanced conformal gripping. *Robotica*, **40**, 1345–1360.

Zheng, J., Xiao, P., Le, X., Lu, W., Théato, P., Ma, C., Du, B., Zhang, J., Huang, Y. & Chen, T. (2018). Mimosa inspired bilayer hydrogel actuator functioning in multi-environments. *Journal of Materials Chemistry C*, **6**, 1320–1327.

Zhou, L., Ren, L., Chen, Y., Niu, S., Han, Z. & Ren, L. (2021). Bio-inspired soft grippers based on impactive gripping. *Advanced Science*, **8**, 2002017.

Appendix A

Supplementary tables

A.1 Parameters used for multi-mode morphing of pneumatic networks using strain-hardening

Symbol	Quantity	Value
w_c^t	Twisting module chamber width (mm)	3
w_s^t	Twisting module side wall thickness (mm)	0.5
d_c^t	Twisting module chamber depth (mm)	16
d_f^t	Twisting module depth wall thickness (mm)	2
h_c^t	Twisting module chamber height (mm)	5.5
h_t^t	Twisting module top wall thickness (mm)	1.5
θ	Twisting angle (rad)	$\pi/4$
w_c^b	Bending module chamber width (mm)	16
w_s^b	Bending module side wall thickness (mm)	1.8
d_c^b	Bending module chamber depth (mm)	15.3
d_f^b	Bending module depth wall thickness (mm)	2.7
h_c^b	Bending module channel height (mm)	3.6
h_b^b	Bending module bottom wall thickness (mm)	1
h_t^b	Bending module top wall thickness (mm)	1
μ_{II}	Elastomer II shear modulus (kPa)	56
μ_{III}	Elastomer III shear modulus (kPa)	80
μ_{VI}	Elastomer VI shear modulus (kPa)	600

Table A.1: Parameters used for pneu-nets of different materials.

Symbol	Quantity	Value
w_c	Chamber width (mm)	5.5
w_s	Side wall thickness (mm)	1.8
d_c^u	Upper chamber depth (mm)	46
d_c^l	Lower chamber depth (mm)	10
d_f	Depth wall thickness (mm)	3
h_c^u	Upper chamber height (mm)	3.8
h_c^l	Lower chamber height (mm)	10.8
h_b	Bottom wall thickness (mm)	3
h_t^u	Upper chamber top wall thickness (mm)	10
h_t^l	Lower chamber top wall thickness (mm)	3
μ_{III}	Elastomer III shear modulus (kPa)	80

Table A.2: Parameters used for pneu-nets of different thicknesses.

Symbol	Quantity	Value
w_c^m	Middle chamber width (mm)	12.1
w_c^l	Lower chamber width (mm)	3.1
w_s^m	Middle chamber side wall thickness (mm)	4
w_s^l	Lower chamber side wall thickness (mm)	8.5
d_c^u	Upper chamber depth (mm)	60
d_c^m	Middle chamber depth (mm)	50
d_c^l	Lower chamber depth (mm)	60
d_f	Depth wall thickness (mm)	5
h_c	Chamber height (mm)	3.9
h_b	Bottom wall thickness (mm)	1.2
h_t	Top wall thickness (mm)	2
μ_{III}	Elastomer III shear modulus (kPa)	80
μ_{VI}	Elastomer VI shear modulus (kPa)	600

Table A.3: Parameters used for pneu-net combinations of different air chamber geometries.

Appendix B

Abstract in Korean

국문초록

변형 경화 또는 상전이를 이용한 공압 기반 다중-모드 모핑 소프트 액추에이터

서울대학교 대학원
기계항공공학부
정한비

요약

본 연구에서는 엘라스토머 재질로 둘러싸인 채널인 뉴-넷을 이용하여 다중 모드 변형이 가능한 소프트 시스템을 개발하였다. 시스템에 연속체 물성 제어 기술 연구를 진행하였고, 하나의 공압 입력으로 두 번 이상 변형할 수 있는 다중 모드 시스템을 엘라스토머의 변형 경화와 상전이를 이용하여 강성을 조절할 수 있는 메커니즘을 규명하였다.

먼저, 엘라스토머의 변형 경화를 이용하여 강성을 조절할 수 있고, 이 현상을 이용하여 다중 모드 모핑이 가능한 조건을 실험적으로 규명하였다. 뉴-넷 채널의 두께와 면적, 재질을 조절해 한 공압 파이프로 두 가지 이상의 변형을 만들어낼 수 있다는 결과를 보였다. 연속체 물성의 성질을 젠트 이론으로 모델링해 이중 변형이 가능하다는 것을 이론적으로 해석하였다. 이 개념을 이용하여 굽힘-굽힘, 팽창-굽힘, 굽힘-회전 운동이 가능한 로봇을 만들었다. 이 시스템을 이용해 두 가지 크기의 물건을 각각 다른 압력에 집을 수 있는 소

프트 그리퍼를 만들고, 내용물이 든 유리병 입구를 폐쇄하고 들어올리거나, 전구를 잡고 돌려서 킬 수 있는 운동을 보였다. 본 연구는 하나의 공압 파이프로만 다중 모드 변형이 가능한 시스템을 제작하는 방법을 제시하였다는 점에서 의의가 있다.

다음으로, 액체-고체의 상전이를 이용하여 재프로그램이 가능한 뉴-넷 시스템을 개발하였다. 뉴-넷 윗 벽에 강성을 제어할 수 있는 레이어를 넣어 액체를 채워 다중층 뉴-넷을 만들었다. 액체는 강성이 없고, 고체는 강성이 있다는 점을 활용해 무수히 많은 변형을 할 수 있는 뉴-넷 시스템을 개발하였다. 강성을 제어하는 다중층에 고체가 들어가 강성을 줄 수 있다는 현상을 빔 이론을 이용하여 규명하였다. 외부 열로 인해 픽셀 단위로 나누어진 시스템을 극부적으로 고체로 채워진 픽셀을 액체로 녹이면, 녹인 디자인에 따라 변형이 달라지는 것을 실험적으로 보였다. 본 연구는 제어하기 쉬운 하나의 공압 파이프로만 무수히 많은 변형을 만들 수 있는 시스템을 개발하였다는 점에서 의의가 있다.

주요어 : 연성 물질, 소프트 액추에이터, 뉴-넷, 다중 모드
학 번 : 2017 – 26227